# Corrosion and Tribological Characteristics of Friction Stir Processed Aluminium Alloy AA5052

B G Yashwanth Kumar[1], R Lokesh Kumar[1], Vaira Vignesh Ramalingam[2], J Kaasi Viswanath[2], R Harikeshava[2], R Padmanaban[2]

Friction stir processing (FSP) is a solid-state and effective process for surface modification of aluminium alloys. In this study the AA5052 alloy, widely used in marine applications, has been subjected to FSP. The FSP trials have been carried out by altering the FSP process parameters (tool rotation speed, tool traverse speed, and shoulder diameter). The friction stir processed specimens have been characterised / tested for microstructure, microhardness, sliding wear, immersion corrosion, and electrochemical corrosion. The hybrid polynomial – radial basis function-based models have been developed to determine the relationship between the process parameters and the evaluated properties. Furthermore, the optimum parameters for obtaining high hardness, wear resistance, and corrosion resistance have been determined. Microstructure evaluation in the friction stir processed specimens has shown refinement and uniform dispersion of β particles throughout the α-Al matrix. The results show that the improvement in properties is a result of the homogeneous dispersion of secondary β phase particles in the matrix. Friction stir processing of AA5052 alloy has improved hardness by ~14.5%, wear resistance by ~83%, and corrosion resistance ~87%. The optimum process window for friction stir processing of AA5052 alloy is tool rotation speed between 500 rpm and 900 rpm, tool traverse speed between 10 mm/min and 30 mm/min, and tool shoulder diameter of 18 mm and 21 mm.

**KEY WORDS**

~ AA5052 alloy
~ FSP
~ Wear
~ Corrosion
~ Hybrid RBF

[1]Queen's University Belfast, School of Mathematics and Physics, Belfast, Northern Ireland, United Kingdom
[2]Amrita School of Engineering, Department of Mechanical Engineering, Coimbatore, Amrita Vishwa Vidyapeetham, India
e-mail: r_vairavignesh@cb.amrita.edu
doi: 10.7225/toms.v11.n02.w03
Received: Jul 19, 2021 / Revised: Nov 26, 2021 / Accepted: Aug 10, 2022 / Published online: Aug 15, 2022

## 1. INTRODUCTION

Aluminium alloys are lightweight alloys which is why they are preferred in aerospace, industrial, and automotive applications. Aluminium alloys exhibit desired engineering properties, such as high strength to weight ratio, good resilience for static and dynamic loading, and high strength at low temperatures, making them suitable for cryogenic applications (extremely low-temperature applications) (Mondolfo, 2013). Aluminium alloys also exhibit good corrosion resistance, because of the formation of a protective thin oxidized layer (Davis, 1993). The formation of thin oxidized layer is attributed to the tendency of aluminum to rapidly react with oxygen. However, the seawater and marine environment are rich in chloride ions. The progressive motion of chloride ions into the aluminium matrix leads to aggravated corrosion (Davis). The segregation of alloying elements and impurities along the grain boundaries forms preferential corrosion sites, which in turn leads to intergranular corrosion. The regions prone to intergranular corrosion accelerate the corrosion rate (Spacht, 1946).

The passivation tendency of alumiinum alloys is attributed to the thin oxidized layer. The absence of re-passivation of thin oxidized layer after chemical dissolution or mechanical damage result in non-passivation of aluminiium alloys. Under such circumstances, pitting corrosion, a localized form of corrosion, dominates the corrosion regime of aluminum alloys. The pits become wide and shallow or narrow and deep which can rapidly perforate the wall thickness of the component made of aluminium alloy. Consequently, the mechanical strength of such materials is compromised. Hence, aluminium alloys that exhibit better pitting resistance are recommended for marine applications. Aluminum alloys that are suitable for marine applications are called marine-grade aluminium alloys. The marine-grade aluminium alloys are confined to the 5XXX series and 6XXX series (Wahid et al., 2020). These alloys are alloyed with magnesium to improve their corrosion resistance to withstand constant exposure to saltwater and moisture. The marine-grade aluminium alloys are used in ship hulls, boat hulls, honeycomb panels for ships, and sheet-metal structures. Some of the conventionally used marine-grade aluminium alloys include AA5052, AA5083, AA5454, AA5754, and AA6061-T6. One of the best marine-grade aluminium alloys is the AA5052 alloy (Mondolfo, 2013).

AA5052 alloy is a non-heat-treatable and widely used alloy for marine applications. The aluminium is alloyed with magnesium and chromium in AA5052 alloy that increases the corrosion resistance. The chromium provides a good amount of corrosion resistance to AA5052 resistance (Sinyavskii and Kalinin, 2005). However, agglomeration of the secondary intermetallic particles accelerates the corrosion rate. Other than corrosion, AA5052 alloys provide high fatigue strength. AA5052 has excellent formability, which makes it ductile and malleable in nature. It has low wear resistance. Also, it has low hardness and strength compared to iron, titanium, and nickel alloys (Howeyze et al., 2018). However, the hardness, strength, wear and corrosion resistance of AA5052 alloy can be improved through certain bulk deformation or processing techniques (Chen et al., 2003).

Alloying, compositing, PVD, and CVD process can be employed for improving the properties of AA5052 alloy (Qin et al., 2019). The corrosion, wear, hardness, and strength of AA5052 could be also improved by bulk deformation processes, like equal channel angular pressing, rolling, extrusion (Chen et al., 2003), drawing, and forging (Seyed Salehi and Anjabin, 2017). AA5052 alloy with H32 work hardening provides good strength (Murugesan et al., 2021), (Shanavas and Dhas, 2017), (Abioye et al., 2019). However, the above processes produce internal residual stress which leads to deterioration in certain properties or failure of the material. Friction Stir Processing (FSP) is a green process, in which no or very minimal residual stress is produced, and no external inclusions are added to the alloy matrix. FSP is a process in which the alloy surface experiences a frictional force by a rotating tool that runs over it. The simultaneous input of strain and frictional heating result in dynamic recovery and recrystallization, that in turn result in grain refinement. By stirring action of the tool, high plastically deformed zones are formed in the stir zone. The plastic deformation of materials increases the dislocation density and vacancy density. The excess dislocations and vacancies are removed during the recovery phenomenon.

Furthermore, the annihilated dislocation structures rearrange into stable arrays and form walls of dislocations (sub-grain boundary). These sub-grains consist of the same phase with different spatial orientation (Vignesh and Padmanaban, 2018a). During the dynamic recrystallization phenomenon, the initial strain causes recrystallization and formation of new strain-free grains (Vignesh and Padmanaban, 2018b). However, additional straining of the material initiates new nucleation sites for recrystallization. Continued application of strain introduces new dislocations into the recrystallized grains that form sub-grains and inhibit further growth of recrystallized grains (Kumar et al., 2011). This series of recrystallization events that modify the microstructure is known as discontinuous dynamic recrystallization (Awad et al., 2018). Further, FSP ensures homogeneous dispersion of second phase intermetallic phases in the stir zone. Hence, the problem related to the brittle inter-dendritic eutectic phases could be eliminated by FSP. The second phase particles influence the low angle boundary (Zener drag effect). Added to this phenomenon, the opposing shear stress, offered by these second phase particles to impede dislocation movement, is significant only if the particle size is few nanometers. The presence of such nano-size particles reduces sub-grain growth and promotes dislocation preservation.

Specifically, in AA5052 alloys, networked Mg2Al3 phase tends to reduce the strength and induce brittle characteristics. The FSP process eliminates the continuous inter-dendritic phases by altering the particles to a spherical shape, which reduces the brittleness. Also, the homogeneous dispersion improves the properties of the alloy (Chanakyan et al., 2021). The uniform distribution of the secondary phase particles improves the properties such as hardness, tensile strength, corrosion resistance, and wear resistance. The homogeneous distribution of the second phase particles restricts the dislocation motion and hence improves the strength and hardness of the alloy. Therefore, FSP can be performed on AA5052 alloy to improve the properties (Dolatkhah et al., 2012).

The quality and properties of the alloy surface depend on the FSP process parameters (Suganya Priyadharshini et al., 2021). The influential FSP process parameters include tool rotation speed (TRS), tool traverse speed (TTS), pin diameter (PD), number of passes, tool tilt angle, shoulder diameter (SD), and pin length. (Hariri et al., 2013) The quality and properties of the alloy could be tuned by selecting the process parameters. Some of the literature on FSP in AA5052 alloy and the influence of process parameters on the properties of AA5052 alloys have been reported. Hariri et al [24] performed the FSP over the AA5052 alloy. The finer grain structure was obtained in the specimen that was processed at a TRS value of 400 rpm and a TTS value of 200 mm/min. Intergranular cracks in the stir zone were observed in the specimen that was processed at TTS values of 80 and 100 mm/min. The results indicate that the desired corrosion resistance and microstructure were obtained in the specimen that was processed at a TRS of 400 rpm and TTS of 250 mm/min. Alex et al (Alex et al., 2020) studied the influence of heat treatment (annealing) on the mechanical and wear behaviour of friction stir processed (FSPed) AA5052 alloy. The FSP technique refined the microstructure and resulted in a better dispersion of β-Mg2Al3 phase particles in the FSPed specimens. The microhardness results reveal that hardness has improved by 16% in the FSPed specimen and 10% in the FSP followed by annealing. The wear rate has shown a decreasing trend with an increase in load for FSPed specimens. The annealing process has reduced the surface hardness, hence the wear rate has been higher in annealed specimens.

Jalili et al (Jalili et al., 2016) carried out both experimental and numerical studies on the FSP of AA5052 alloy, with a simultaneous cooling system using an impinging jet of CO2 gas. The experimental analysis reveals that the cooling process has reduced the stir-zone distortion and peak temperature by 58% and 34% respectively. The numerical simulations through finite element modelling analysis has revealed the residual stresses to be reduced by 50% as a result of the cooling system. Kumar et al (Kumar et al., 2011) performed FSP on Equal Channel Angular Pressed (ECAP) AA5052 alloy sheet. The grain refinement and high angle grain boundaries fraction changed from 15% in ECAP to approximately 71% after FSP. However, yield strength and ultimate tensile strength were reduced by 34% and 21% respectively in FSPed specimens. Improvement in strain hardening behaviour and the lower recovery rate were observed in FSPed specimens compared to ECAP specimens. Prabhakar et al (Prabhakar et al., 2018) fabricated AA5083 surface metal matrix composite

reinforced with fly-ash by FSP. The corrosion rate of the composite (0.135 mm/year) was 8% higher than that of the FSPed specimen (0.015 mm/year). The corrosion performance of AA5083/fly-ash composite was not favourable in corrosive environments in comparison with FSPed AA5083 alloy. Similar results were reported by Yuvaraj et al (Yuvaraj and Aravindan, 2015) who fabricated AA5083 surface composite reinforced with B4C particles by FSP.

Sharifitabar et al (Sharifitabar et al., 2011) fabricated AA5052 alloy reinforced with Al2O3 nano-ceramic particle (50 nm in size) through the FSP method. The effect of the number of FSP passes on the microstructure and tensile strength were investigated. The microstructure of the composite after four FSP passes revealed the presence of submicron-sized grains. Al2O3 clusters with a mean size of 70 nm were obtained after four passes. The tensile strength and elongation improved to 118% and 165% respectively after four FSP passes in the fabricated composite. Similarly, Ashjari et al (Ashjari et al., 2015) investigated the process environment's influence on the mechanical properties of Al2O3 reinforced AA5083 nano-composite manufactured by the FSP technique. Both the air-cooled and underwater FSP were performed to fabricate the composite. The microstructure of underwater FSP revealed agglomeration of reinforcements in the specimens fabricated with a few passes, hence an increase in the number of passes reduced agglomerations. The average grain size of underwater FSP and air-cooled FSP was found to be 2.5 μm and 6 μm respectively. The yield strength of the underwater FSP was 15% higher than the air-cooled FSP technique. Dolatkhah et al (Dolatkhah et al., 2012) fabricated AA5052 alloy reinforced with SiC particles (size ranging from 5 μm to 50 nm) by means of the FSP method. The microstructure refinement (average grain size of 0.9 μm) and a uniform distribution were achieved in the specimen processed with TRS of 1120 rpm and TTS of 80 mm/min. The microhardness and wear rate of the AA5052 alloy, improved to 55% and 10% respectively after four FSP passes, was attributed to the fine refinement of grains in the course of FSP. Similarly, Bodaghi et al (Bodaghi and Dehghani, 2017) also investigated the effects of SiC nano-particle addition in the FSP of AA5052 alloy. The nanoparticles, which acted as nucleation sites, had a significant effect on grain refinement (mean grain size reduced from 36 μm to 5 μm). The higher microhardness in the stir zone was attributed to the presence of hard SiC particles. The one-pass FSPed specimen exhibited lower tensile strength as a result of the agglomeration of particles. Wear resistance was lesser due to the improper distribution of nanoparticles in the stir zone. This has resulted in more weight loss of the specimens in the course of the wear test.

Huang et al (Huang et al., 2016) also studied the effect of TRS on microhardness and microstructure of FSPed AA5056/SiC cold sprayed composite. The microstructure revealed the presence of fine grains in the AA5056 matrix, that in turn was attributed to the large plastic deformation during FSP. The FSPed specimens contained homogeneous distribution of fine SiC particles in the matrix. The size of the reinforcements was reduced from 12.5 μm to 6.5 μm at TRS of 600 rpm and 12.5 μm to 7 μm at TRS of 1400 rpm. The microhardness of the FSPed specimens showed a general softening profile with a decrease of Vicker's microhardness from 144HV to 110 HV. Likewise, Byung-Wook et al (Byung-Wook et al., 2012) fabricated AA5083/SiC composite through FSP and investigated its microstructure and mechanical properties. The number of passes affected the particle distribution and grain refinement in the Al matrix. After one pass, the SiC particles were entangled in the upper side of the stir zone. However, after two passes, a uniform distribution of SiC particles and grain refinement was achieved. The AA5083 composite region exhibited 13% higher hardness than the Friction stir welded AA5083 alloy, attributed to the larger grain size in AA5083 alloy.

Shahraki et al (Shahraki et al., 2013) fabricated AA5083/ZrO2 nanocomposite by FSP technique. The microstructure and mechanical properties of the nanocomposite were investigated. The microstructure revealed the presence of recrystallized equiaxed grains, and similar size particle distribution was observed. The hardness of the FSPed composite was 30% higher than the as-received AA5083 alloy. The ultimate tensile strength of the composite was 10% higher than the FSPed specimen. Similarly, Mirjavadi et al (Mirjavadi et al., 2017) also fabricated AA5083 surface composite reinforced with ZrO2 nano-particles by FSP. The effect of the number of passes on the microstructure, microhardness, tensile strength, and wear properties were investigated. A refined

microstructure (equiaxed grains) with uniform distribution of reinforcements was observed in FSPed specimens with 2, 4, 6, and 8 passes. Hardness and tensile strength were higher in 2, 4, 6, and 8 passes of FSPed specimens, attributed to the presence of fine equiaxed grains. However, the wear rate showed a decreasing trend with an increase in the number of passes of FSP. The significant reduction in wear rate was a result of high hardness achieved after multi-pass stirring and load-bearing capacity of the ZrO2 nano-particles.

The previous research work indicates that the FSP of AA5052 alloy improves hardness, strength, wear, and corrosion resistance. However, optimization of FSP process parameters yields the most desirable properties in AA5052 alloy, which is experimentally very challenging. Hence, researchers utilise techniques such as statistical modeling to determine the FSP process parameters that would result in multiple desirable properties. Soft computing is one of the allied-flourishing areas of statistical modelling, that includes Sugeno (Jayakarthick et al., 2018), fuzzy (Barath et al., 2018, Kiruthi Murugan et al., 2018), radial basis function (RBF) (Anil Kumar et al., 2019, Murugan et al., 2018), artificial neural network (ANN) (Vaira Vignesh and Padmanaban, 2018, Prudhvi Sai et al., 2021), and hybrid functions. In addition, the statistical modelling shows the relationship between the FSP process parameters and the property achieved in the specimen. Literature on FSP soft computing models is explored below. Vignesh et al (Vignesh and Padmanaban, 2018a) analysed the effect of FSP parameters on the intergranular corrosion susceptibility of aluminium alloy AA5083. Experimental results revealed that FSP had significantly reduced the corrosion susceptibility in the nitric acid mass loss test of AA5083 aluminium alloy. Among the developed soft computing models, the Sugeno Fuzzy system showed a minimum error percentage. The modelling results showed that AA5083 alloy that was FSPed at a TRS of 1300 rpm, TTS of 60 mm/min, and SD of 21 mm were least susceptible to intergranular corrosion. Vignesh et al (Ramalingam and Ramasamy, 2017) fabricated AA5083 alloy via the FSP technique and investigated the corrosion behavior. The microstructural observation of the FSPed alloy revealed uniform distribution of the secondary phase particles in the FSPed zone. The polynomial radial basis function model was developed and the process parameters were optimized. The results showed that the corrosion resistance of the FSPed specimens was far improved than the base material. The specimen FSPed at TRS of 1000 rpm, SD of 18 mm, and TTS of 45 mm/min resulted in a maximum corrosion resistance.

The existing literature shows that FSP is an efficient technique to improve the microstructure and the properties like hardness, strength, wear, and corrosion. It is also evident that the statistical modelling substantiates the optimum FSP process parameters for maximising the properties. Research work on optimising the mechanical, tribological, and corrosion characteristics of FSPed AA5052 alloy simultaneously was seldom discussed in the open literature. In this study, the hardness, wear rate, corrosion rate (immersion and electrochemical studies), and corrosion potential in the FSPed AA5052 alloy were determined. Also, a relationship was established between FSP process parameters (tool rotation speed, tool traverse speed, shoulder diameter) and the different properties through a hybrid mathematical model. The optimum FSP process parameters for multiple desirable properties in AA5052 alloy were also determined.

## 2. MATERIALS AND METHODS

### 2.1. Material

Aluminium alloy 5052 workpieces were sliced into specimens of the dimension of 150 mm ×50 mm ×4 mm, using a hydraulic shear cutting machine and employed for this research work. The edges of the plates were made parallel to provide proper clamping in the fixture, which is made of mild steel. The composition of Al 5052 alloy is given in **Table 1**.

| Alloy | Si | Fe | Cu | Mn | Mg | Cr | Al |
|---|---|---|---|---|---|---|---|
| AA5052 | 0.115 | 0.372 | 0.017 | 0.055 | 2.363 | 0.191 | Balance |

Table 1. The elemental composition of AA5052 alloy.

## 2.2. Friction Stir Processing

The workpieces were cleaned, and the grease was removed using acetone before the FSP trial. The workpieces were FSPed using an electrically controlled (potentiostat) friction stir welding setup at Amrita Vishwa Vidyapeetham. The tool used for FSP had a cylindrical profile of 18 mm in diameter. The pin diameter and height were found to be 5 mm and 3.8 mm, respectively. The dwell time was about 60 s. The face-centred central composite design was used to proceed with the experimental process by changing the process parameters (tool rotation speed, tool traverse speed, and shoulder diameter). This method was more efficient because of the augmentation of centre points to the axial points in the cubical design. The tool rotation speed was changed between 500 rpm (low) and 900 rpm (high); tool traverse speed was varied between 10 mm/min (low) and 30 mm/min (high); shoulder diameter was varied between 12 mm (low) and 18 mm (high). The specimens were given a specimen code, their respective process parameters values being tabulated in Table 2

| Sl. | Specimen code | TRS | TTS | SD | Microhardness (HV) | | | | | Corrosion rate | Corros. Potential | Corrosion rate | Wear Rate |
|---|---|---|---|---|---|---|---|---|---|---|---|---|---|
| | | rpm | mm/min | mm | -2 | -1 | 0 | 1 | 2 | mm/yr | V | mpy | g/Nm |
| 01 | FSP01 | 500 | 10 | 12 | 70.5 | 66.3 | 74.2 | 71 | 67.4 | 0.426913 | -0.965 | 2.39E+00 | 3.09026E-07 |
| 02 | FSP02 | 900 | 10 | 12 | 64.1 | 65 | 67.1 | 62.1 | 63.4 | 0.373328 | -1.288 | 8.30E-01 | 2.42807E-07 |
| 03 | FSP03 | 500 | 30 | 12 | 64.9 | 63.3 | 62.9 | 63.7 | 66.6 | 0.356794 | -0.908 | 3.32E+02 | 3.20063E-07 |
| 04 | FSP04 | 900 | 30 | 12 | 63.5 | 59.7 | 65.9 | 62.2 | 61.4 | 0.909377 | -1.075 | 5.79E+00 | 2.86953E-07 |
| 05 | FSP05 | 500 | 10 | 18 | 57.8 | 60.5 | 58 | 57.4 | 58.6 | 0.082412 | -1.377 | 2.99E+00 | 1.03745E-06 |
| 06 | FSP06 | 900 | 10 | 18 | 55.7 | 58.1 | 59.3 | 60.1 | 60.1 | 7.439486 | -0.999 | 1.92E+00 | 2.20733E-08 |
| 07 | FSP07 | 500 | 30 | 18 | 65.4 | 65.6 | 64.8 | 62.7 | 62.2 | 0.194831 | -1.465 | 4.54E+00 | 4.08356E-07 |
| 08 | FSP08 | 900 | 30 | 18 | 58.9 | 61.3 | 59.9 | 60.4 | 59.9 | 0.568813 | -1.215 | 7.97E-01 | 4.6354E-07 |
| 09 | FSP09 | 500 | 20 | 15 | 64 | 64.8 | 63.3 | 63 | 62.8 | 0.222758 | -1.430 | 3.28E+00 | 4.3043E-07 |
| 10 | FPS10 | 900 | 20 | 15 | 68.6 | 67.1 | 70.5 | 67.4 | 70.5 | 0.201455 | -1.381 | 8.97E+00 | 4.19393E-07 |
| 11 | FSP11 | 700 | 20 | 12 | 72.4 | 72.8 | 74.1 | 72.5 | 72.2 | 0.32013 | -1.425 | 4.98E+00 | 3.42136E-07 |
| 12 | FSP12 | 700 | 20 | 18 | 71.9 | 72.9 | 70.2 | 78.6 | 75.3 | 2.532464 | -1.267 | 3.25E+00 | 6.07016E-07 |
| 13 | FSP13 | 900 | 10 | 15 | 67 | 61.5 | 63 | 66.8 | 65 | 0.491077 | -1.205 | 2.06E+00 | 3.20063E-07 |
| 14 | FSP14 | 700 | 30 | 15 | 63.7 | 62.8 | 63.8 | 64.6 | 65.9 | 0.678053 | -1.397 | 9.03E+00 | 1.03745E-06 |
| 15 | FSP15 | 700 | 20 | 15 | 60.7 | 60.8 | 59.2 | 60.1 | 59.9 | 0.204367 | -1.289 | 1.78E+00 | 8.2775E-07 |

Table 2. The specimens with specimen code and their respective process parameters.

## 2.3. Microstructure

The FSPed specimens, along with base material, were cut along the transverse section and mounted using a cold setting compound. The specimens were prepared according to the standard ASTM E3-11. The specimens were ground using 400, 600, 800, 1000 grit emery papers. Then a mirror polish was obtained by using a disc polisher containing velvet cloth and alumina colloidal suspension. The polished specimens were cleaned using acetone and etched for 25 s using Keller's reagent (190 ml of distilled water, 5 ml of nitric acid, 3 ml of hydrochloric acid, and 2 ml of hydrofluoric acid). The microstructural observation was carried out using an optical microscope (Maker: Carl Zeiss; Model: Axiovert 25).

## 2.4. Microhardness

The FSPed specimens were prepared as per the standard ASTM E3-11. The Vickers micro-hardness measurements were taken along the transverse section using a micro-hardness tester with a diamond indenter (Maker: Mitutoyo, Model: MVK-H1) as per ASTM standard E384. The load applied was 9.81 N (1 kg) for a period of 15 s. The hardness was measured at 15 different locations and the average hardness was reported for each set of parameters.

## 2.5. Tribological Characterization

The specimens of dimension 10 mm × 10 mm were sliced from the FSPed workpiece and they were polished as per ASTM E3-11 standard. They were mounted in a cylindrical tube of dimension φ 12 mm and length 50 mm using a cold setting compound. The wear rate was determined using a pin-on-disc apparatus (Maker: DUCOM, Model: TR20LE). The grease was removed from the specimen surface using acetone. The specimen weight was measured using a precision weighing balance with the least count of 0.0001 g. The wear testing parameters were as follows: sliding velocity of 0.005 m/s, and a constant normal load of 2 kg. The wear rate of the specimens was calculated from **Equation (1)** (Arun Kumar et al., 2021, Premkumar et al., 2021, Bhardwaj et al., 2021).

$$Wear\ Rate = \frac{\Delta M}{L \times SD} \tag{1}$$

Where ΔM is a mass loss, L is the load applied and SD is the sliding distance.

## 2.6. Corrosion Testing

### 2.6.1. Immersion Corrosion Testing

The specimens of dimension 10 mm × 10 mm were taken from FSPed workpieces. The specimens were polished as per the standard ASTM E3-11. The specimens were cleaned and the dirt was removed using ethanol. The immersion corrosion test was conducted as per ASTM G31-72 standard. The weight of the specimens was measured using a precision balance of resolution 0.0001 g. The immersion tests were performed in a saltwater solution (3.5% of NaCl solution). The saltwater solution was prepared by mixing 3.5 g of NaCl in 100 ml of distilled water. The temperature of the solution was maintained using a water bath, fitted with a digital temperature controller. After the immersion period, the specimens were ultrasonicated in ethanol for 3 minutes to remove the corrosion products. The specimens were allowed to dry and weighed in precision balance to calculate the mass loss.

The corrosion rate was calculated using **Equation (2)** (Ramalingam et al., 2019, Vignesh et al., 2018, Vaira Vignesh et al., 2020).

$$Corrosion\ rate = \frac{K \text{ x } \Delta M}{A \text{ x } T \text{ x } D} \quad (2)$$

Where K = 8.76 x 104, ΔM is mass loss, A is surface area, T is time, and D is the density of AA5052 alloy.

### 2.6.2. Electrochemical Corrosion Testing

The specimens of dimensions 50 mm × 10 mm × 4 mm were prepared from the FSPed workpieces for the corrosion test and polished as per ASTM E3-11 standard. The specimens were exposed to an area of 1 mm2 and the remaining area was isolated using insulation tape. The potentiodynamic polarization method was used to analyse the electrochemical corrosion potential and electrochemical corrosion rate of the FSPed specimens in a saltwater solution. The potentiodynamic polarization was carried out in an electrochemical workstation (Maker: CH Instruments, Texas, USA, Model: CHI 660C). The electrolyte was prepared by mixing 3.5 g of sodium chloride (NaCl) in 100 ml of distilled water. The pH was measured to be 7.8, using the digital pH meter. The various electrodes used in the electrochemical cell setup are discussed as follows: the test specimen acts as the working electrode, the standard calomel electrode acts as the reference electrode, and the platinum rod is used as the counter electrode. The open-circuit potential (OCP) was established for 90 minutes. After stabilisation, the potentiodynamic polarisation measurements were started. The electrochemical corrosion test was performed in the potential range of -1.5 V to -0.5 V at a scan rate of 5 mV/s. The corrosion tests were conducted at a temperature range of 45 ± 0.1oC. The electrochemical cell setup consisted of a water bath to maintain the temperature of the electrolyte and a thermometer was used for continuous monitoring of temperature. The current sensitivity was chosen as 10-2μA. The electrochemical corrosion tests results were obtained in the form of Tafel plots. The corrosion potential (Ecorr in volts) was calculated from the intersection of the slopes of anodic (βa in volts/decade) and cathodic (βc in volts/decade) polarisation curves. The corrosion current density was derived from the Tafel constants. The **Equation (3)** and **Equation (4)** (Vignesh et al., 2020, Vaira Vignesh et al., 2019a, Vaira Vignesh et al., 2019b, Vaira Vignesh et al., 2020) were used to calculate the corrosion current density and corrosion rate respectively.

$$i_{corr} = \frac{\beta_a * \beta_c}{2.3(\beta_a + \beta_c)} * \frac{1}{R_p} \quad (3)$$

$$corrosion\ rate = \frac{k * i_{corr} * E'}{A * \rho} \quad (4)$$

Where, $R_p$ is the polarisation resistance in Ω (ohms), k is a constant, $i_{corr}$ is the corrosion current in Ampere, $E'$ is equivalent weight in grams, A is the area exposed in $cm^2$ and ρ is the density of the specimen material in g $cm^{-3}$.

## 2.7. Hybrid Polynomial - Radial Basis Function

A hybrid model was developed from the integration of a radial basis function and a linear function. The model correlates the input variables (TRS, TTS, and SD) response output variables (microhardness, wear rate, immersion corrosion rate, and corrosion potential, and electrochemical corrosion rate). The function which returns any real value or any function that follows the **Equation (5)** is known as Radial Basis Function (RBF).

$$(x, c) = (||x - c||) \quad (5)$$

In the above Equation (5), x is the variable and c is the centre point. There are many RBF types, like gaussian, multi-quadratic, inverse quadratic, inverse multi-quadratic, poly-harmonic spline, and thin-plate spline. In this current study, we have utilised multi-quadratic type RBF. This type of RBF uses the characteristic equation for approximating the function shown in **Equation (6)**,

$$RBF = y(x) \sum_{i=1}^{n} w(i) \times \varphi(|x - x(i)|) \tag{6}$$

X is the approximant value and w is the weight value calculated by iterations. The characteristic equation of linear- RBF is given by **Equation (7).**

$$z = LF + RBF \tag{7}$$

Here z is a liable variable, LF is a linear function.

## 2.8. Surface Morphology, Elemental Composition and Phase Composition Analysis

A high-resolution Scanning Electron Microscope (SEM) (Maker: Zeiss Sigma) has been used in this study for the surface morphology observation of the worn-out and corroded specimens. The energy dispersive X-ray electron spectroscope (Maker: Bruker) has been utilised for performing elemental composition analysis of worn-out and corroded specimens. The phase composition of the specimen has been determined by an X-ray diffractometer (Maker: Rigaku). The XRD spectra have been obtained by means of Cu-Kα radiation in continuously scanning mode, at a scan rate of 0.5°/min.

# 3. RESULTS AND DISCUSSION

## 3.1. Microstructure

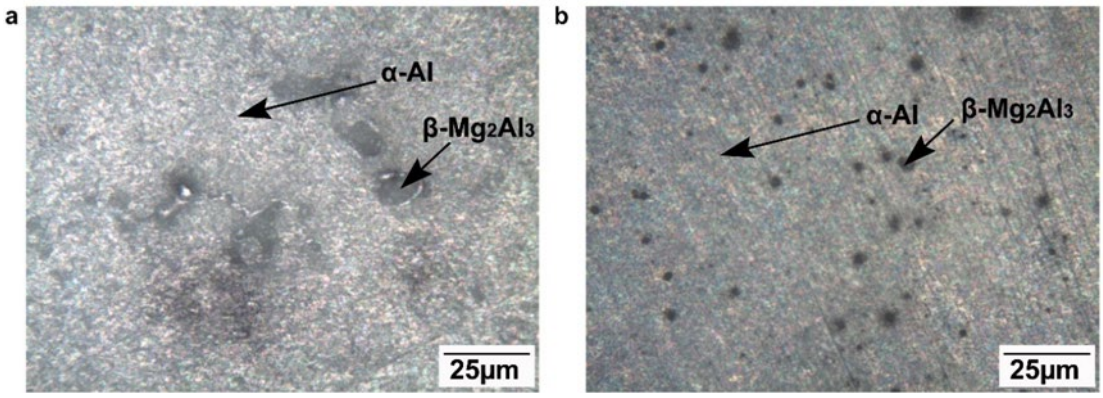


Figure 1. The microstructure of the a) base material and b) FSPed specimen.

It is evident from the phase diagram of the Al-Mg alloy system that the primary phase of AA5052 alloy is an α-Al phase and the secondary intermetallic phase is $Mg_2Al_3$. The microstructure of the base material is shown in **Figure 1(a).** The microstructure of the base material illustrates the inhomogeneous distribution of coarse β-$Mg_2Al_3$ phase particles. The typical microstructure of the FSPed specimen is depicted in **Figure 1(b).** The microstructure reveals the refinement of β particles. Also, they are uniformly dispersed throughout the α-Al matrix. The uniform distributions of β phase particles have been attributed to the continuous stirring action in the course of the friction stir process. The reasonable dynamic recovery and recrystallization have resulted in grain refinement and the formation of sub-grain boundaries. The XRD analysis has been carried out on the base

material, as well as the FSPed specimen. **Figure 2 (a)** and **Figure 2 (b)** have confirmed the presence of primary phase (α-Al) and a secondary intermetallic phase (β-$Mg_2Al_3$) in the AA5052 base material and the FSPed specimen. No characteristic changes have been observed in the phases of the FSPed specimens.

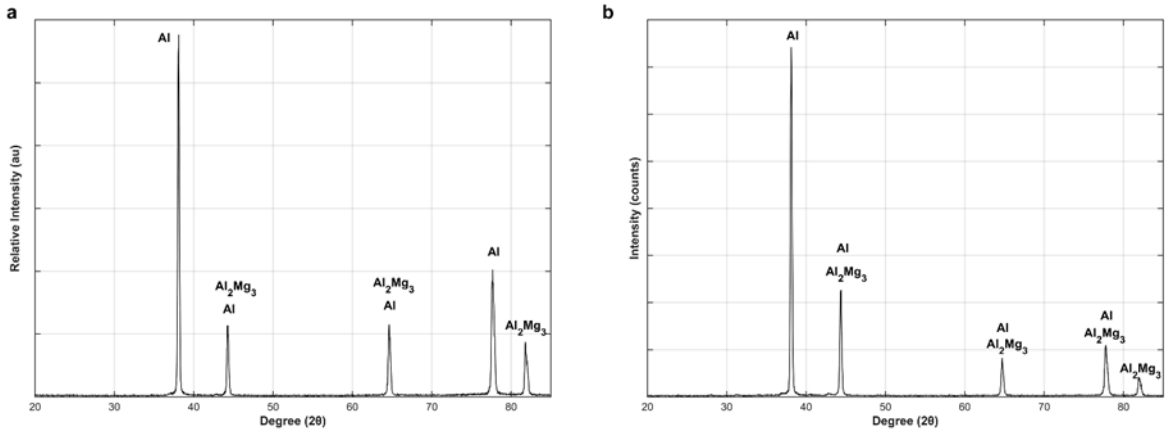


Figure 2. The XRD analysis of the a) base material and b) FSPed specimen.

## 3.2. Microhardness

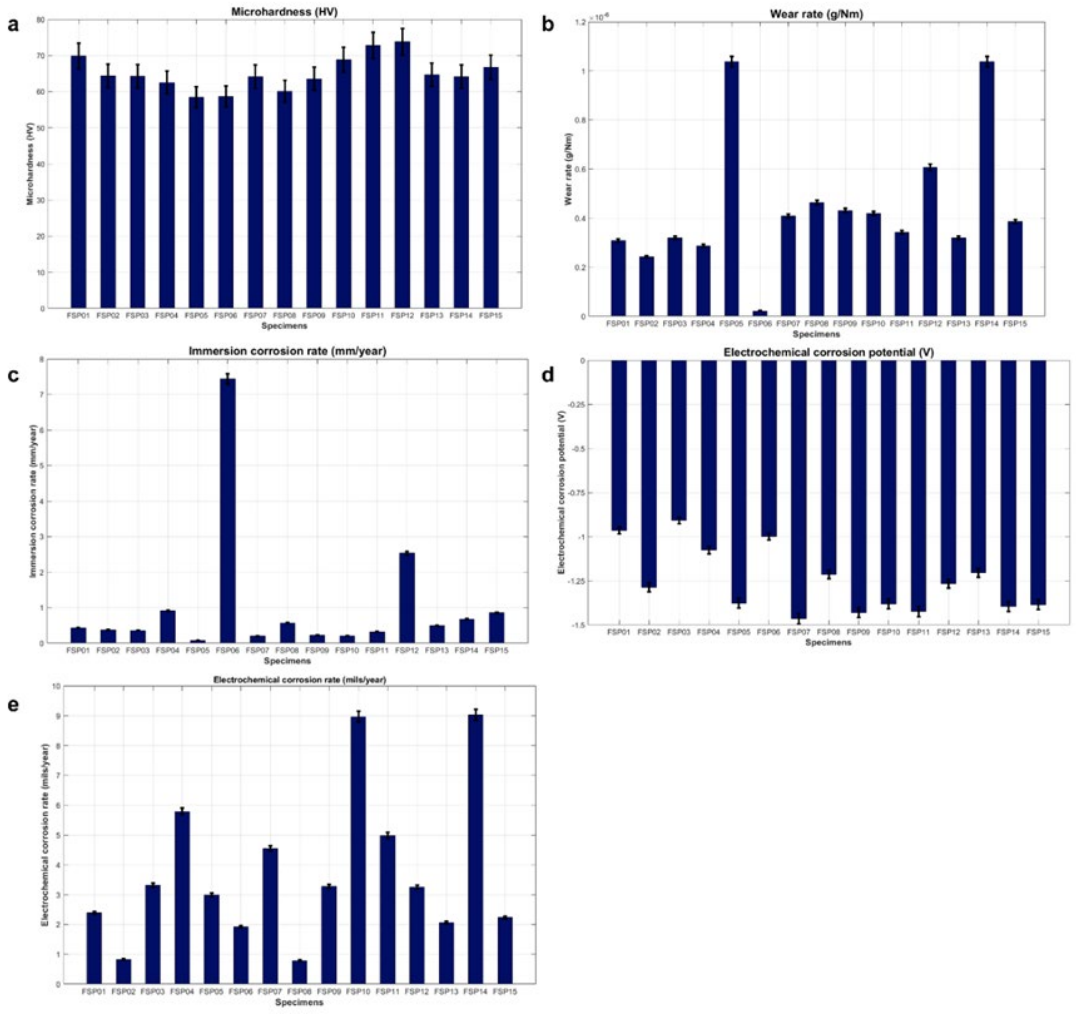


Figure 3. The bar graphs of a) microhardness b) wear rate c) Immersion corrosion rate d) electrochemical corrosion potential and e) electrochemical corrosion rate.

The Vickers microhardness test has been performed on both the base material and the FSPed specimens. The average microhardness of the base material has been found to be 64.47 HV. The average microhardness values of the FSPed specimens, fabricated with different process parameters, drawn as a bar graph, are shown in **Figure 3 (a).** A maximum average microhardness value of 73.78 HV has been observed in the specimen FSP12, fabricated at TRS of 700 rpm, TTS of 20 mm/min, and SD of 18 mm. A minimum average microhardness value of 58.46 HV has been observed in the specimen FSP05, fabricated at TRS of 500 rpm, TTS of 10 mm/min, and SD of 18 mm.

The adequate dynamic recovery and recrystallization have resulted in the refinement of grains, homogeneous dispersion of β phase particles, and formation of sub-grain boundaries (dislocation tangles) in the specimen FSP12. Hence, the microhardness of the specimen FSP12 has been seen to be 12.61% higher than that of the base material. The specimen FSP05 have shown lesser microhardness values than the base material. This may be ascribed to the non-uniform distribution of β phase particles, agglomeration of β phase particles caused because of the insufficient heat flow, and increased grain growth.

| Sl. | Model | Equation |
|---|---|---|
| 1 | Microhardness | $106.6271 - 91.91375 \times SD - 68.44201 \times TRS + 18.0413 \times TTS + RBF_1$ |
| 2 | Immersion Corrosion rate | $8.9257 - 5.1093 \times SD - 4.7809 \times TRS + 2.7095 \times TTS + RBF_2$ |
| 3 | Corrosion potential | $-2.5639 - 0.19589 \times SD + 0.18042 \times TRS - 0.34356 \times TTS + RBF_3$ |
| 4 | Corrosion rate | $54.5909 + 61.852 \times SD - 55.6035 \times TRS - 54.3311 \times TTS + RBF_4$ |
| 5 | Wear rate | $6.281\,E-07 + 7.004 \times 10^{-7} \times SD - 5.5185 \times 10^{-9} \times TRS + 3.3031 \times 10^{-7} \times TTS - 7.2113 \times 10^{-7} \times SD^2 - 2.345 \times 10^{-7} \times SD \times TRS - 3.7722 \times 10^{-7} \times SD \times TTS - 2.0319 \times 10^{-7} \times TRS^2 + 2.6764 \times 10^{-7} \times TRS \times TTS + 7.9032 \times 10^{-8} \times TTS^2 + RBF_5$ |

Table 3. Model equations for different hybrid models.

A hybrid model has been developed to analyse the influence of TRS, TTS, and SD on microhardness, and the model equation is given in **Table 3**. The radial basis function network uses a multi quadratic kernel. The centres, global width, and the regulation parameter are shown in **Table 4**.

| Sl. | Model | RBF Number | Centers | Global width | Regularization parameter |
|---|---|---|---|---|---|
| 1 | Microhardness | RBF 1 | 4 | 3.9192 | 0.0001 |
| 2 | Immersion Corrosion rate | RBF 2 | 4 | 0.47768 | 0.0001 |
| 3 | Corrosion potential | RBF 3 | 3 | 0.15851 | 0.0001 |
| 4 | Corrosion rate | RBF 4 | 4 | 3.0893 | 0.0001 |
| 5 | Wear rate | RBF 5 | 4 | 3.6206 | 0.0001 |

Table 4. The RBF number, centers, global width, and regularization parameters for different models.

The $R^2$ and RMSE values of the developed model are given in **Table 5**. The parameters indicate the model to be statistically significant. Hence, the model has been used to create contour plots that describe the relationship between the process parameters and microhardness.

| Sl. | Model | $R^2$ | RMSE |
|---|---|---|---|
| 1 | Microhardness | 0.718 | 2.61 |
| 2 | Immersion Corrosion rate | 0.999 | 0.094 |
| 3 | Corrosion potential | 0.945 | 0.982 |
| 4 | Corrosion rate | 0.991 | 0.959 |
| 5 | Wear rate | 0.784 | 2.102E-7 |

Table 5. $R^2$ and RMSE values for the models.

### 3.2.1. Effect of process parameters on the microhardness

#### *3.2.1.1. Effect of TRS and SD*

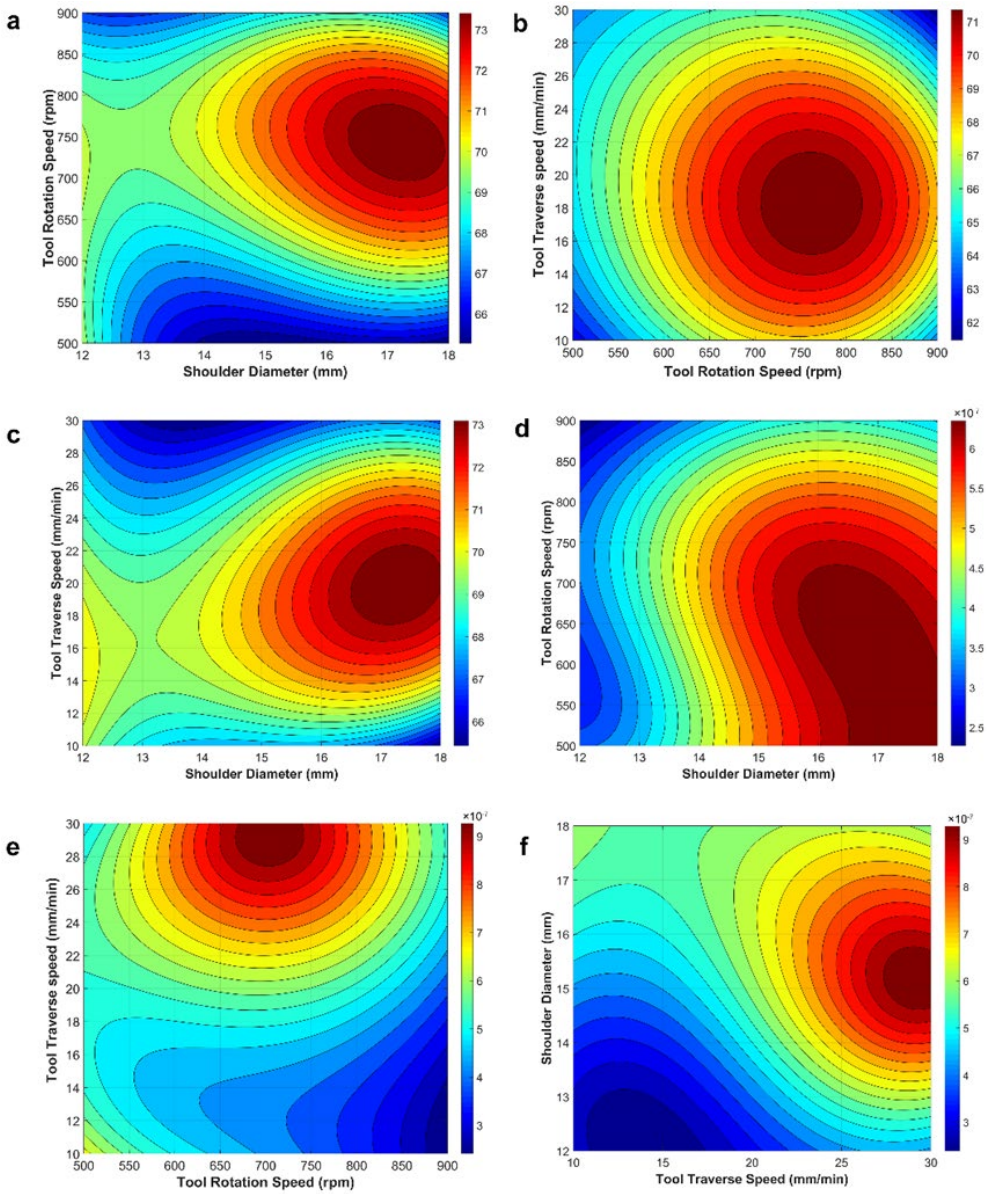


Figure 4. The contour plots of hardness a) TRS vs SD b) TRS vs TTS c) TTS vs SD and wear rate d) TRS vs SD e) TRS vs TTS f) TTS vs SD.

The microhardness variation to the FSP process parameters TRS and SD is patently shown as a contour plot in **Figure 4 (a)**. The microhardness shows a bell-shaped Gaussian trend as TRS increased and for all SD values. Going through the contour plot, it may be seen that a maximal microhardness above 73 HV has been obtained at a TRS range of 700 rpm to 800 rpm and an SD range of 16 mm to 18 mm. The least microhardness below 66 HV has been observed at a TRS below 500 rpm and above 900 rpm and for all SD values.

#### 3.2.1.2. Effect of TRS and TTS

The influence of TRS and TTS on the microhardness of the FSPed specimens is displayed as a contour plot in **Figure 4 (b).** The microhardness has a bell-shaped Gaussian shift as the TRS, and TTS increased. From the contour plot, the highest value of microhardness above 71 HV has been reported at a TRS range of 700 rpm to 820 rpm and a TTS range of 15 mm/min to 22 mm/min. Lower values of hardness less than 63 HV have been observed in the specimens processed at TRS values below 550 rpm and above 850 rpm and at TTS values below 12 mm/min and above 28 mm/min.

#### 3.2.1.3. Effect of TTS and SD

The effect of TTS and SD process parameters on the microhardness is described as a contour plot in **Figure 4 (c).** There is a bell-shaped Gaussian trend observed in microhardness as the value of TTS increases and for all SD. The high value of microhardness above 73 HV has been observed in the specimens at a TTS range of 18 mm/min to 22 mm/min and at an SD range of 16 mm to 18 mm. Minimal microhardness value below 66 HV has been identified at TTS values below 10 mm/min and above 28 mm/min and for all SD values.

#### 3.2.1.4. Inference

During FSP, the rotating FSP tool is traversed under the action of load. Hence, the shoulder surface and pin of the FSP tool generate frictional heat in the workpiece. The magnitude of heat generated by the shoulder and pin is given by **Equation (8)** and **Equation (9)** respectively.

$$q_{shoulder}(r,T) = \begin{cases} \mu(F_n/A_s)\omega r, if\ T < T_{melt} \\ 0, \qquad\qquad if\ T > T_{melt} \end{cases} \tag{8}$$

$$q_{pin}(T) = \begin{cases} \dfrac{\boldsymbol{\mu}}{\sqrt{\mathbf{3}(\mathbf{1}+\boldsymbol{\mu})^2}} r_p \omega Y(T), if\ T < T_{melt} \\ 0, \qquad\qquad\qquad if\ T > T_{melt} \end{cases} \tag{9}$$

As observed, processing of specimens at a high TRS would generate more frictional heat between the contact surface (tool and workpiece) than at a low TRS. A low TTS causes high heat input because of the prolonged frictional heating effect in the FSP zone. Similarly, processing of specimens at high SD would generate more frictional heat than at low SD. As described in the previous research work (Jalili et al., 2016, Vignesh et al., 2016, Padmanaban et al., 2014), effective recovery and recrystallization (both static and dynamic) occur if the workpiece has a desired level of heat and strain. A high heat input causes coarsening of grains after recovery and recrystallization phenomenon. Also, the heat input influences the precipitation of secondary intermetallic phases in the matrix. Besides, FSP at high TRS results in turbulent flow of material and inhomogeneous distribution of the β phase particles. Also, low TTS ineffectively changes material transfer from advancing to retreating side. The process parameters TRS, TTS, and SD influence the microstructural evolution in the FSPed zone, resulting in a complex phenomenon.

The following grain refinement mechanisms improve the microhardness of the FSPed zone: fine grains, homogeneous dispersion of fine β particles, and formation of sub-grain structures (dislocation-based). Fine grains have more grain boundaries than coarser grains. These grain boundaries inhibit the propagation of dislocations, thereby increasing the hardness. The homogeneous dispersion of fine β particles in the FSPed region improves hardness by restricting the dislocation motions. The β particles are harder than the primary α-Al., thereby enabling a dislocation motion at a large force to break or circumvent the β particles. Therefore, a homogeneous dispersion of β particles improves the microhardness of the FSPed zone. Also, sub-grain structures, formed after recovery and recrystallization, inhibit the dislocation motion, causing an increase in microhardness.

An excess (high TRS, low TTS, high SD) or restraint (low TRS, high TTS, low SD) heat input causes ineffective recovery and recrystallization and hence lacks grain refinement mechanisms. This in turn leads to decreased microhardness of the FSPed zone. FSP of specimens at low TRS or high TTS results in assorted distribution of the β phase particles, reducing in turn the hardness of the FSPed zone. Cumulatively, the decrease in microhardness is attributed to ineffective recovery and recrystallization or coarsening of grains or heterogeneous distribution or agglomeration of β phase particles in the FSPed zone. The FSP process window, aimed at improving the microhardness of the AA5052 alloy, is as follows: TRS between 700 rpm and 800 rpm; TTS between 16 mm/min to 22 mm/min; SD between 16 mm and 18 mm.

## 3.3. Tribological Characterization

### 3.3.1. Wear rate

The wear rate of the FSPed specimens for different process parameters has been calculated through the sliding wear test performed using the pin on the disc apparatus. The average wear rate of the base material was $1.3056 \times 10^{-7}$ g/Nm. The wear rate, calculated for the FSPed specimens by varying process parameters, is shown as a bar graph **Figure 3 (b).** The maximum wear rate of $10.3745 \times 10^{-7}$ g/Nm has been observed in the specimens FSP05 and FSP14. The FSP05 has been processed at TRS of 500 rpm, TTS of 10 mm/min, SD of 18 mm, and the other specimen FSP14 has been processed at TRS of 700 rpm, TTS of 30 mm/min, and SD of 15 mm. The minimum wear rate of $0.2206 \times 10^{-7}$ g/Nm has been observed in the specimen FSP06, fabricated at a TRS of 900 rpm, TTS of 10 mm/min, and SD of 18 mm. The minimum wear rate in the specimen FSP06 is attributed to the grain refinement and homogeneous dispersion of β phase $Mg_2Al_3$ particles. The static and dynamic recovery and recrystallization at adequate amounts have resulted in the formation of sub-grain boundaries in the FSP06 specimen. Hence, the wear rate has decreased by 83.10% in the specimen FSP06, in comparison with the base material. The specimens FSP05 and FSP14 tend to have a larger wear rate due to the heterogeneous distribution of coarser secondary phase particles in the matrix. A hybrid model has been developed to analyse the influence of TRS, TTS, and SD on wear rate, and the model equation is given in **Table 3**. The radial basis function network uses a multi quadratic kernel. The centres, global width and, the regularization parameter, lambda, are given in **Table 4**. The $R^2$ and RMSE values of the developed model are given in **Table 5**. The parameters indicate the developed model to be statistically significant. Hence, the model was utilised to generate contour plots that describe the relationship between the process parameters and wear rate.

#### *3.3.1.1. Effect of process parameters on the wear rate*

- **Effect of TRS and SD**

The wear rate deviation, with variation in TRS and SD, is shown as a contour plot in **Figure 4 (d)**. The contour graph depicts an increasing trend of wear rate, as the SD increased. The maximum wear rate value was observed when the specimens were processed in the TRS range of 500 rpm to 700 rpm and the SD above 16

mm. It was observed that the TRS did not significantly influence the wear rate, without a simultaneous increase in SD above 14 mm. The least wear rate has been noticed for the specimen processed in the TRS range of 500 rpm to 700 rpm and SD range of 12 mm and 13 mm, or TRS range of 770 rpm to 900 rpm and SD range of 12 mm and 14 mm.

- **Effect of TRS and TTS**

The relationship between TRS and TTS on the wear rate of the FSPed AA5052 is depicted as a contour plot in **Figure 4 (e).** The contour plot exhibits a rising trend of wear rate as TTS increases. The wear rate has been high in the specimens processed at the TRS range of 650 rpm to 750 rpm and TTS range of 27 mm/min to 30 mm/min. The least wear rate has been found in the specimens processed at TTS below 16 mm/min and TRS above 800 rpm. The wear rate has been reduced at a high TTS of 30 mm/min by maintaining the TRS value either above 800 rpm or below 600 rpm.

- **Effect of TTS and SD**

The change in wear rate of the FSPed specimens with respect to TTS and SD is shown as a contour plot in **Figure 4 (f).** A decreasing trend has been observed in the wear rate of the specimens processed at low SD. Also, high wear has been observed in the specimens processed at the TTS range of 25 mm/min to 30 mm/min at the SD range from 14 mm to 17 mm. Besides, lesser wear rate has been observed in the specimens processed at TTS ranging from 10 mm/min to 20 mm/min and SD ranging from 12 mm to 15 mm.

- **Inference**

The material of high hardness with less wear rate is most preferred for engineering applications. The material with high hardness usually exhibits less wear rate, which is why the hard material would not wear off easily. Obviously, the material with low hardness tends to have a high wear rate, therefore the material with a low hardness index wears away at a fast rate in the course of contact motion. At times, materials with high hardness also exhibit a high wear rate. That could be attributed to the abrasive wear mechanism, in which the chipped out hard base material acts as a third-body between the contact surfaces, thereby leading to a high wear rate.

The wear rate has been mainly influenced by the grain refinement mechanism in the stir zone. The homogeneous distribution of β-phase fine $Mg_2Al_3$ particles in α phase matrix and the appearance of fine grains are attributed to high hardness. Such microstructural configuration prevents the dislocation motion and increases the hardness, which in turn results in a low wear rate. On the other hand, grain coarsening and heterogeneous dispersion of β-phase $Mg_2Al_3$ particles tend to soften the specimens, leading to a high wear rate in the specimens.

The high heat input (high TRS, low TTS, high SD) or low heat input (low TRS, high TTS, low SD), influenced by FSP parameters, contributes towards the lack of effective recovery and recrystallization. This ineffective recovery and recrystallization lead to coarsening of grains and disordered distribution of β-phase $Mg_2Al_3$ particles, thereby paving the way for a deterioration of properties in the material. At higher SD and high TRS, excessive heat is introduced in the specimen, followed by grain growth after recovery and recrystallization. The coarsening of grains results in an excessive wear rate, whereas at high TTS, low heat input results in an ineffective recovery and recrystallization phenomenon, leading to a deterioration of properties in FSPed specimens. By comparing the wear rate variation with respect to TRS, TTS, and SD, it is evident that processing of specimens at TRS above 800 rpm, TTS ranging from 10 mm/min to 14 mm/min, and SD ranging from 12 mm to 13 mm results in a superior wear resistance.

### 3.3.1.2. Worn surface morphology and elemental composition analysis

The worn surface morphology of the base material has been discussed in our earlier research work (Arjun et al., 2019). The typical worn surface morphology of the FSPed specimen FSP06 having a mild wear rate is shown in **Figure 5 (a-c)**. The spalling defect, caused by the removal of material as particles, is shown in **Figure 5 (a)**. The cyclic impact centred on the contact region, known as delamination, is shown in **Figure 5 (a).** The bright spots are the wear debris and the furrows, caused by the dragging of particles in the course of the wear test, as depicted in **Figure 5 (b).** The galling effect, which may be attributed to the adhesive phenomenon, occurs during the sliding contact between the surfaces. The galling effect and the presence of a deep groove are shown in **Figure 5 (c).**

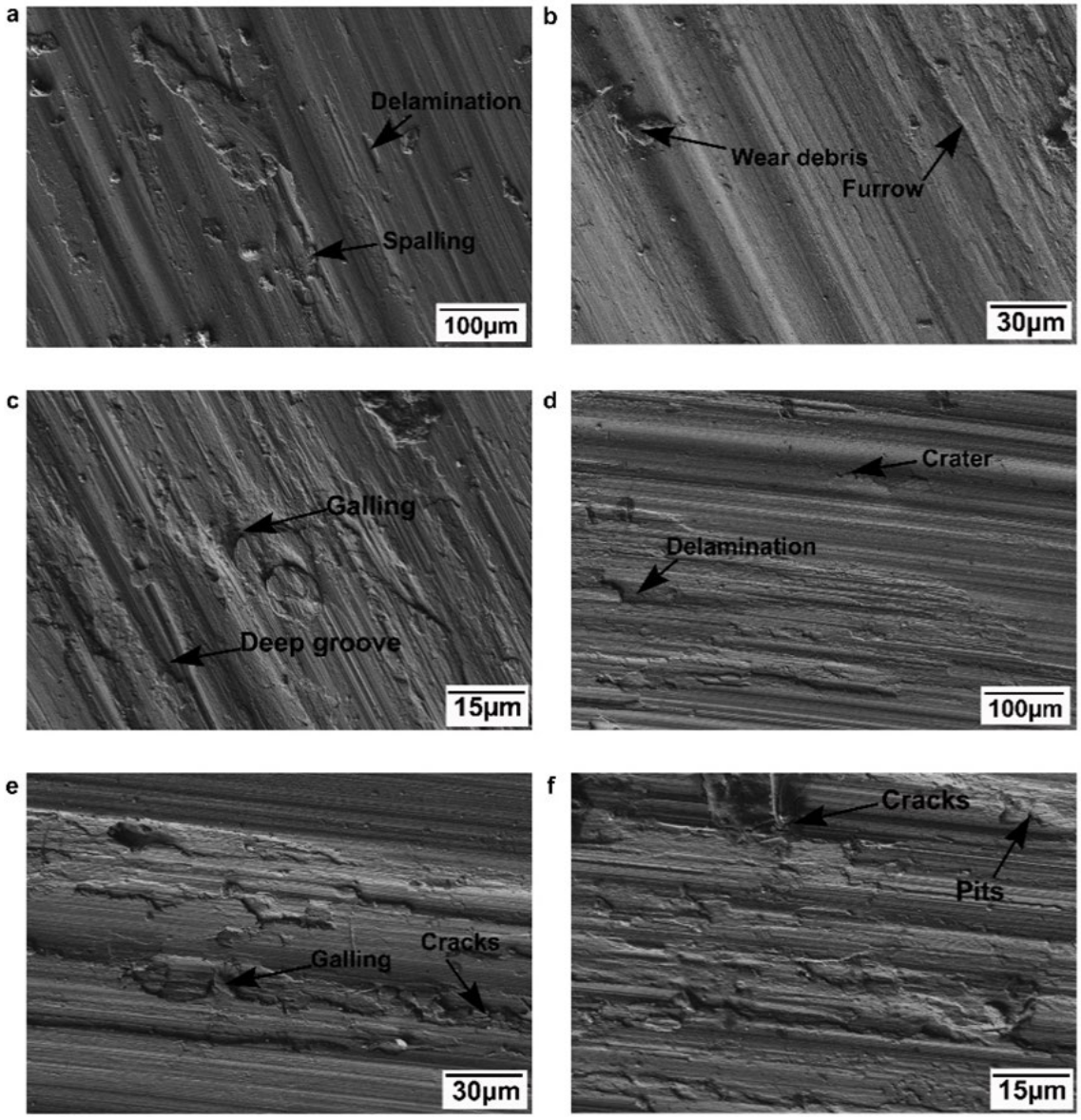


Figure 5. (a-c) The worn surface morphology of the FSP06 specimen with mild wear rate. (d-f) The worn surface morphology of the FSP14 specimen with severe wear rate.

**Figure 5 (d-f)** shows the worn surface morphology of the FSPed specimen FSP14, exhibiting a severe wear rate. The delamination was caused by layer-by-layer removal of the specimen by the counter disc. Besides delamination, the presence of a crater is shown in **Figure 5 (d).** The secondary cracks, formed in the worn

specimen, and galling defect are shown in **Figure 5 (e)**. In addition to cracks, the presence of pits is shown in **Figure 5 (f).** EDS spectrograph of the FSPed specimen FSP06 with a mild wear rate is shown in **Figure 6 (a)**. The elements including Al of 90.88%, O of 6.50 %, and Mg of 2.62% have been present. The low concentration of O indicates partial oxidative wear in the FSP06 specimen. **Figure 6 (b)** shows the EDS spectrograph of the worn-out FSPed specimen FSP14. The elements including Al of 74.17%, O of 23.17%, and Mg of 2.66% have been present in the FSP14 specimen. The high concentration of oxygen content confirms the oxidative wear in the FSP14 specimen.

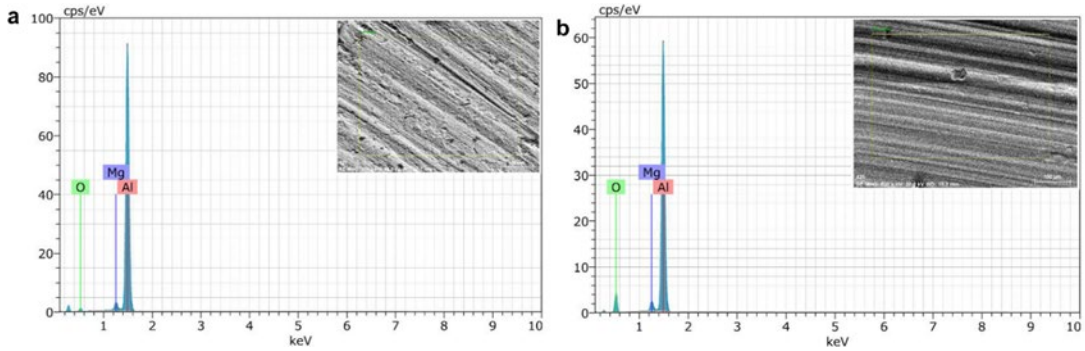


Figure 6. The wear elemental composition images of the FSPed specimens a) FSP06 and b) FSP14.

## 3.4. Corrosion Characterisation

### 3.4.1. Immersion Corrosion

The immersion corrosion rate of the FSPed specimens has been calculated through an immersion corrosion test performed in saltwater (3.5 g of NaCl in 100 g of distilled water). The average immersion corrosion rate of the base material obtained was 0.0932 mm/yr. The immersion corrosion rate, calculated for the FSPed specimens at various parameters, is shown as a bar graph shown in **Figure 3 (c).** Among the FSPed specimens, a maximum immersion corrosion rate of 7.4394 mm/year has been recorded in the specimen FSP06, processed at TRS of 900 rpm, TTS of 10 mm/min, and SD of 18 mm. The corrosion rate of the specimen FSP06 has been 98 % higher than the base material. The least immersion corrosion rate value of 0.0824 mm/year is observed in the FSP05 specimen. The process parameters, at which the FSP05 specimen was fabricated, have been TRS of 500 rpm, TTS of 10 mm/min, and SD of 15 mm. The corrosion rate of the specimen FSP05 has been 13 % lower than the base material. A hybrid model was developed to analyse the influence of TRS, TTS, and SD on immersion corrosion rate, and the model equation is given in **Table 3.** The radial basis function network uses a multi quadratic kernel. The centres, global width, and the regularization parameter (lambda) are given in **Table 4**. The $R^2$ and RMSE value of the developed model is given in **Table 5**. The parameters indicate that the model was statistically significant. Hence, the model was utilised to generate contour plot, describing the relationship between the process parameters and the immersion corrosion rate.

#### *3.4.1.1. Effect of process parameters on the immersion corrosion rate*

- **Effect of TRS and SD**

The immersion corrosion rate of the FSPed specimens with variation in TRS and SD is displayed as a contour plot in **Figure 7 (a)**. The immersion corrosion rate was observed to have an increasing trend, with a simultaneous increase in TRS and SD. The contour graph clarifies that the maximum immersion corrosion rate was seen in the specimens FSPed at a TRS range of 800 rpm to 900 rpm and SD range of 16.8 mm to 18 mm. A minimum immersion corrosion rate was obtained in the specimens processed at the TRS range of 500 rpm to 650 rpm, and SD ranging from 12 mm to 15 mm.

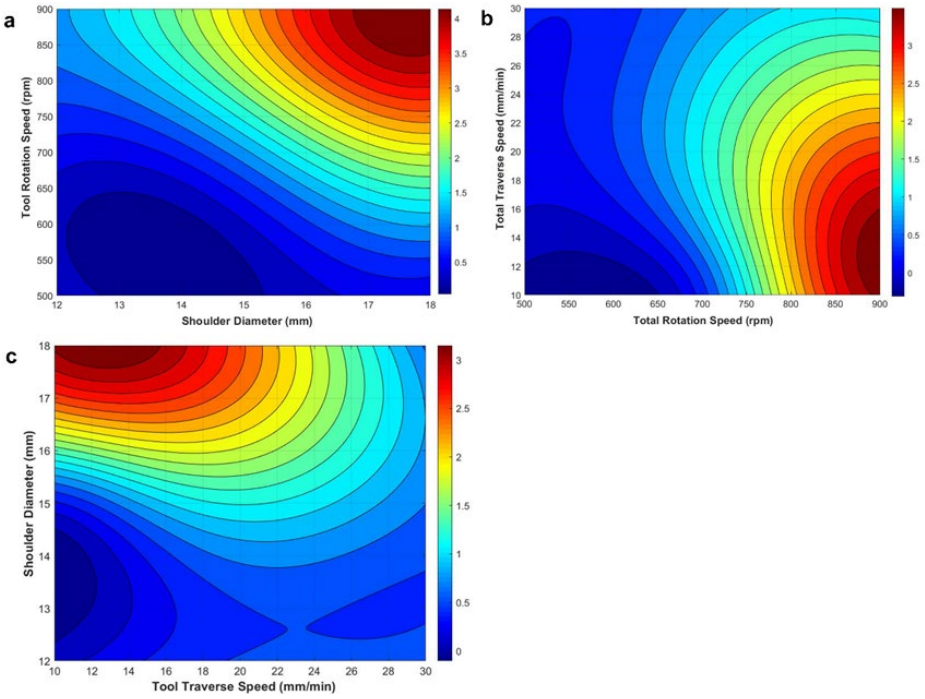


Figure 7. The contour plots of Immersion corrosion rate a) TRS vs SD b) TRS vs TTS and c) TTS vs SD.

- **Effect of TTS and TRS**

The influence of TRS and TTS on the immersion corrosion rate of the FSPed specimens is shown as a contour plot in **Figure 7 (b).** The contour plot depicts an increasing trend of immersion corrosion rate with an increase in TRS. The high immersion corrosion rate has been observed in the specimen processed at TRS of 800 rpm to 900 rpm and TTS range of 10 mm/min to 16 mm/min. However, the least immersion corrosion rate was identified at TRS ranging from 500 to 650 rpm and TTS range of 10 to 13 mm/min. In addition, the immersion corrosion rate was low in the FSPed specimens at all TTS values for TRS below 650 rpm.

- **Effect of TTS and SD**

The variation in the immersion corrosion rate of the specimens with change in TTS and SD are displayed as a contour plot in **Figure 7 (c).** The contour plot shows an increasing trend as the SD increases. A higher immersion corrosion rate has been observed in the specimen processed in the SD range of 17 mm to 18 mm and the TTS range of 10 mm/min to 15 mm/min. The least immersion corrosion rate was observed in the specimens FSPed at SD ranging from 12.5 mm to 14.5 mm at TTS range of 10 mm/min to 12 mm/min. The immersion corrosion rate was low for specimens that were processed using SD lesser than 15 mm irrespective of TTS.

- **Inference**

The high or low immersion corrosion rate observed in the FSPed specimens can be explained in terms of morphology, distribution of β phase particles, and grain size. From the results obtained, the immersion corrosion rate has been less in most of the FSPed specimens that exhibit fine dispersion of β phase particles. The fine dispersion of β phase particles has caused less intergranular corrosion (IGC) effect. This characteristic tendency has reduced the corrosion rate in FSPed specimens. However, agglomeration of β phase particles has resulted in more IGC effect in some of the FSPed specimens. Also, the specimens with fine grains contain a large number of grain boundaries. The increased number of grain boundaries paves the way for high activity, and hence increase the immersion corrosion rate in the FSPed specimens.

The results have shown the FSP of the specimens at high TRS, high SD, and low TTS, to be leading to excessive heat input in the stir zone. The high heat input has resulted in grain growth, followed by recovery and recrystallization. Therefore, the immersion corrosion rate of the FSPed specimens, processed at a high TRS, high SD, and low TTS, has been higher. Besides, FSP of specimens at low TRS, low SD, and high TTS has introduced a low heat input in the stir zone. The low heat input has caused ineffective recovery and recrystallization. At low TRS and high TTS, β phase particles have been distributed in a non-uniform pattern. Hence, the immersion corrosion rate is higher when there is either an excessive or restrained heat input. By comparing the corrosion rate variation with respect to TRS, TTS, and SD, the process window for minimizing the corrosion rate of the specimens has been determined as follows: TRS ranging from 500 rpm to 650 rpm, TTS ranging from 10 to 12 mm/min, and SD range of 12.5 to 14.5 mm.

#### *3.4.1.2. Immersion corrosion surface morphology and elemental composition analysis*

The surface morphology of the corrosion specimens has been observed by means of a high-resolution scanning electron microscope. The typical surface morphology of the FSP06 specimen with a high corrosion rate after the immersion corrosion test is shown in **Figure 8 (a)** and **Figure 8 (b).** Many bright regions (white marks) and relatively few dark regions have been observed throughout the entire surface of the specimen FSP06. The bright spots represent the corrosion products formed over the surface of the specimen in the course of the immersion corrosion test. The dark region indicates either the un-affected sites or fresh sites of the specimen after the dissolution of corrosion products in the electrolyte solution. The formation of aluminium hydroxide in the intermediate stage of immersion corrosion has caused the bulging on the surface of the specimen, which in turn is responsible for cracking on the surface. The presence of a large fraction of corroded and cracked sites attests to the high corrosion rate of the specimen. The typical surface morphology of the FSP05 specimen with less corrosion rate is shown in **Figure 8 (c)** and **Figure 8 (d)**. Comparatively, less bright regions and more dark regions have been observed in the specimen FSP05. The less corrosion rate has been attested by the absence of a large fraction of corroded and cracked sites.

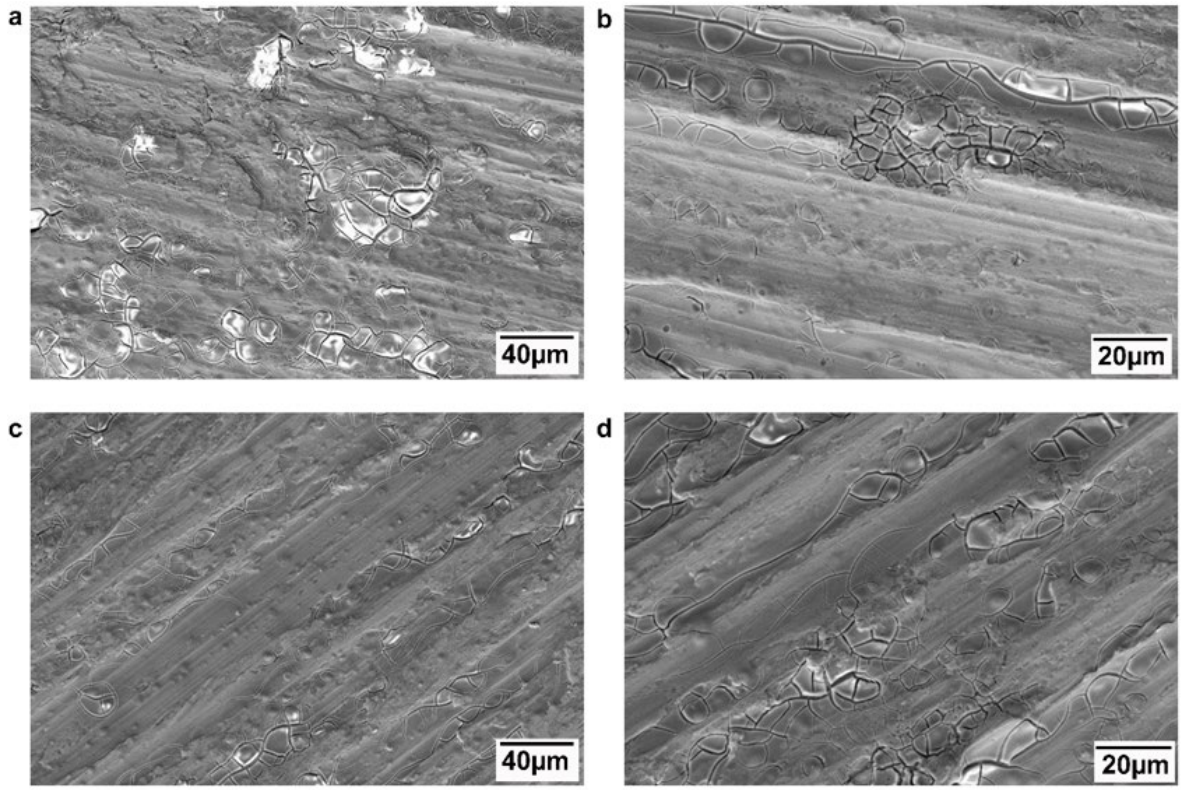


Figure 8. The surface morphology of immersion corroded FSPed specimens a) & b) FSP06; c) & d) FSP05.

The EDS spectrograph of the corroded specimen FSP05 with less corrosion rate is shown in **Figure 9 (a).** The EDS spectrograph confirms the presence of elements Al (77.67 wt.%), O (20.12 wt.%), Mg (2.02 wt.%), and Na and Cl in negligible amounts. The possible corrosion products are aluminium chloride ($AlCl_3$) and aluminium oxide ($Al_2O_3$). The dissolution of corrosion product $AlCl_3$ into solution results in fewer counts for Cl in the EDS spectrograph. The oxygen peaks indicate the presence of the typical adherent oxide film of aluminium oxide ($Al_2O_3$) in the aluminium alloy. The EDS spectrograph of the FSP06 specimen with a high corrosion rate indicates the presence of Al (75.29 wt.%), O (22.35 wt.%), Mg (2.21 wt.%), and a negligible quantity of Na and Cl, as shown in **Figure 9 (b).** Similar to the base material, the FSPed specimens show the presence of a high amount of oxygen and a minimal quantity of chloride. Hence, the corrosion mechanism of the base material and FSPed specimens could be similar. Similar corrosion characteristics were reported for the base material in the previous research work (Sherif and Narayan, 1989).

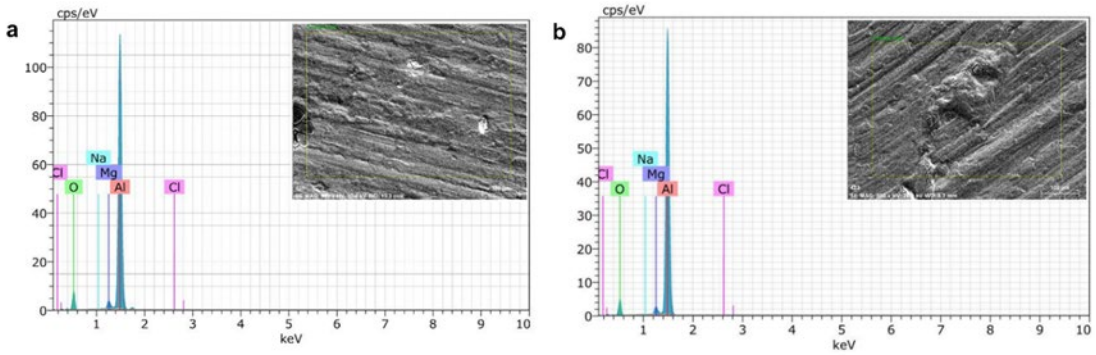


Figure 9. The immersion corrosion elemental composition images of FSPed specimen a) FSP05 & b) FSP06.

### 3.4.1.3. Immersion corrosion mechanism

The presence of an adherent layer of aluminium oxide on the FSPed specimen decreases the corrosion rate. However, defective sites in the aluminum oxide layer expose aluminium to saltwater in the course of the immersion test. The reaction of aluminium with the saltwater solution during the immersion corrosion test is shown in **Equation (10)**, **Equation (11)**, and **Equation (12)**. The aluminium in the course of immersion dissociates into $Al^{3+}$ ions, as shown in **Equation (10)**. The presence of dissolved $O_2$ enables the formation of hydroxide $OH^-$ ions, as shown in **Equation (11)**.

$$Al \rightarrow Al^{3+} + 3e^- \tag{10}$$

$$2H_2O + 4e^- + O_2 \rightarrow 4OH^- \tag{11}$$

$$Al^{3+} + 3OH^- \rightarrow Al(OH)_3 + 3e^- \tag{12}$$

$$Al(OH)_3 + 3Cl^- \rightarrow AlCl_3 + 3(OH)^- \tag{13}$$

$$2Al + 3H_2O \rightarrow Al_2O_3 + 6H^+ + 6e^- \tag{14}$$

The saltwater solution is considered electrolyte-rich in $H^+$, $Na^+$, $OH^-$, and $Cl^-$ ions. The aluminium ions $Al^{3+}$ (FCC crystal structure) react with $OH^-$ions in the electrolyte solution to form of $Al(OH)_3$ aluminium hydroxide, as shown in **Equation (12)**. The formation of intermediate compound $Al(OH)_3$, bulging the specimen surface. $Al(OH)_3$ , has a limited solubility in water and is practically insoluble (solubility product, $K = 3 \times 10^{-34}$). The cumulative formation of $Al(OH)_3$ aids the surface crack formation and propagation. However, highly reactive $Cl^-$ ions, having smaller radius, penetrate $Al(OH)_3$. The $Al(OH)_3$ has readily reacted with $Cl^-$ions. This reaction of chloride ions with $Al(OH)_3$ results in the formation of corrosion product $AlCl_3$, as shown in **Equation (13)**.

$AlCl_3$ has a solubility of 45.8 grams in 100 ml at 20°C. Hence, the $AlCl_3$, which is the corrosion product formed during the immersion corrosion, is soluble in a saltwater solution. This causes the surface to be exposed to further corrosion. The aluminium also reacts with saltwater to form aluminum oxide ($Al_2O_3$) film on the surface, as shown in **Equation (14)** (Sherif & Narayan, 1989).

### 3.4.2. Electrochemical corrosion

The electrochemical corrosion characteristics of the FSPed specimens have been studied using a potentiodynamic corrosion test. The corrosion potential, corrosion current, and corrosion rate have been calculated for each specimen. The typical Tafel plot of the FSPed specimen and methodology to extract the corrosion potential and corrosion current in the Tafel region are shown in the **Figure 10**.

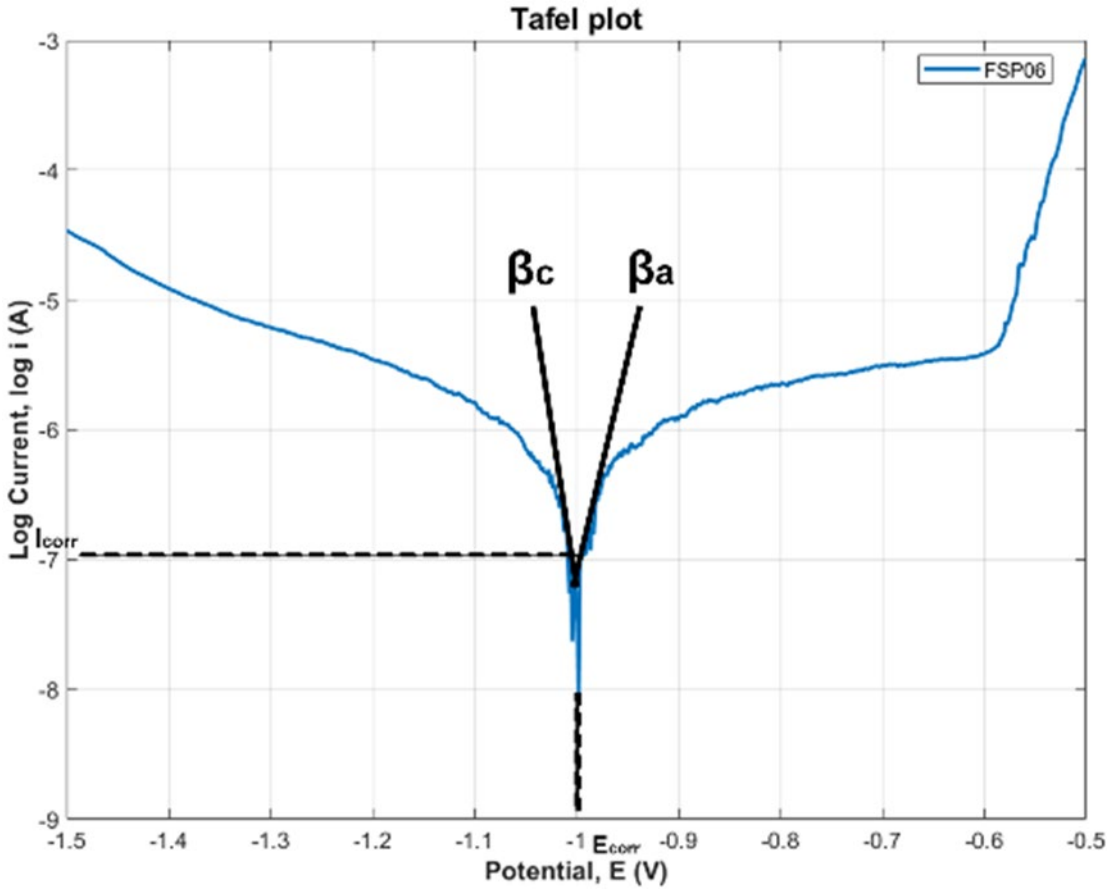


Figure 10. The Tafel plot of FSPed specimen.

#### *3.4.2.1. Corrosion Potential*

The corrosion potential for the base material and FSPed specimens have been found through the potentiodynamic corrosion test. The average corrosion potential of the base material has been observed as -1.279 V. The corrosion potential of the FSPed specimens, processed at different process parameters, are shown as a bar graph in **Figure 3 (d)**. The homogeneous dispersion of fragmented β phase particles may have contributed towards more cathodic corrosion behaviour. A severe agglomeration, causing intergranular corrosion and an unordered mixture of the β phase particles, could have resulted in a more pronounced anodic corrosion behaviour.

A more positive corrosion potential of -0.908 V has been found in the specimen FSP03, fabricated at TRS of 500 rpm, TTS of 30 mm/min, and an SD of 12 mm. More negative corrosion potential of -1.465 V has been observed in the specimen FSP07 processed at TRS of 500 rpm, TTS of 30 mm/min, and SD of 18 mm. A soft computing hybrid model has been generated to examine the effect of TRS, TTS, and SD on corrosion potential. The model equation is given in **Table 3**. The radial basis function network utilises a multi quadratic kernel. The centres, global width, and the regularization parameter, lambda, are given in **Table 4**. The $R^2$ and RMSE values of the developed model are given in **Table 5**. The parameters indicate that the model is statistically significant. Hence, the model was used to create contour plots that describe the relationship between the process parameters and the corrosion potential.

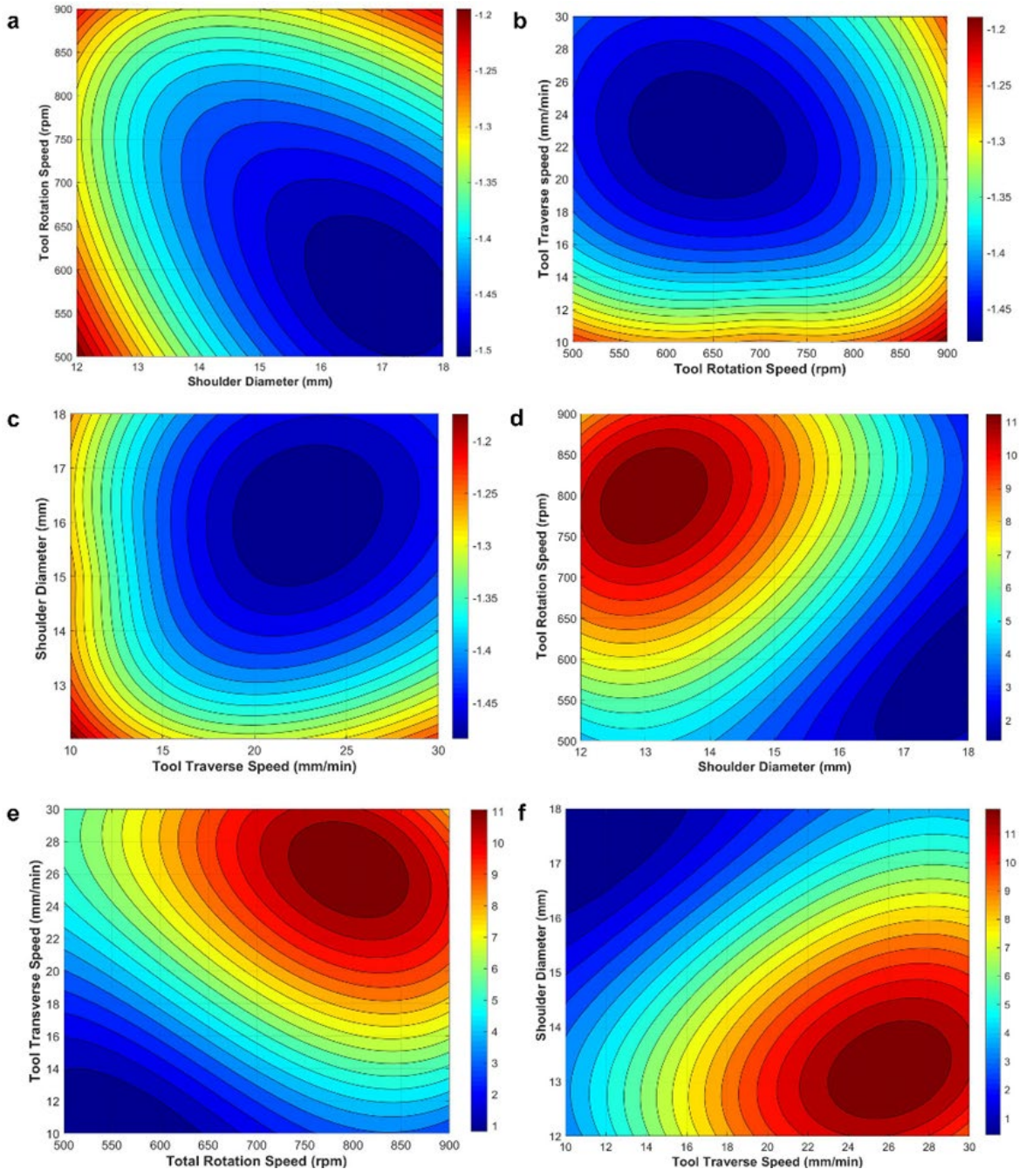


Figure 11. The contour plots of corrosion potential a) TRS vs SD b) TRS vs TTS c) TTS vs SD and corrosion rate d) TRS vs SD e) TRS vs TTS f) TTS vs SD

**Effect of process parameters on the corrosion potential:**

- **Effect of TRS and SD**

The influence of the FSP process parameters TRS and SD on the corrosion potential is depicted in the contour plot **Figure 11 (a).** The corrosion potential has exhibited a decreasing trend as SD increased. The more anodic corrosion potential below -1.5 V has been observed in the specimens processed at a TRS below 650 rpm and SD above 16 mm. The more cathodic potential above -1.25 V has been observed in the specimens processed at TRS above 800 rpm and below 600 rpm, and at SD values below 13 mm and above 17 mm.

- **Effect of TRS and TTS**

The impact of the FSP process parameters TRS and TTS on the corrosion potential is shown as a contour plot in **Figure 11 (b)**. The inverted bell-shaped curve trend has been exhibited by the corrosion potential with an increase in TTS for all TRD. A more anodic corrosion potential below -1.45 V has been observed in the specimens processed at a TRS range of 550 rpm to 750 rpm and a TTS range of 19 mm/min to 27 mm/min. A more positive corrosion potential (above -1.25 V) has been observed in the specimens processed with TTS values less than 12 mm/min and above 28 mm/min (at any value of TRS).

- **Effect of TTS and SD**

The effect of TTS and SD on the corrosion potential of the FSPed specimens is displayed in **Figure 11 (c)**. An inverted bell-shaped trend can be observed, as the values of SD have increased and for all TTS values. A more negative corrosion potential below -1.45 V has been observed in the specimens processed at a TTS value ranging from 19 mm/min to 27 mm/min and an SD value ranging from 15 mm to 17 mm. More cathodic corrosion potential of above -1.25 V has been observed in the specimens processed at all TTS with SD value below 12 mm; and TTS below 11 mm/min at all SD.

### *3.4.2.2. Electrochemical corrosion rate*

The electrochemical corrosion rate for the base material and the FSPed specimens have been determined through the potentiodynamic corrosion test. The extraction of data from the Tafel region was discussed in our earlier research work (Ramalingam et al., 2019). The corrosion rate for the FSPed specimens is shown as a bar graph in **Figure 3 (e)**. The base material had an electrochemical corrosion rate of 3.83 mils/year. The highest electrochemical corrosion rate of 9.03 mils/year was observed in the specimen FSP14 that was processed at TRS of 700 rpm, TTS of 30 mm/min, and SD of 15 mm. A minimum electrochemical corrosion rate of 0.79 mils/year was observed in the specimen FSP08, processed at TRS, TTS, and SD of 900 rpm, 30 mm/min, and 18 mm respectively. It can be said that the electrochemical corrosion rate of the base material is seen to be 79.37% higher than that of the specimen FSP08.

A hybrid model has been created to study the consequence of TRS, TTS, and SD on electrochemical corrosion rate. The model equation is shown in **Table 3**. The radial basis function network uses a multi quadratic kernel. The centres, global width, and the regularization parameter, lambda, are shown in **Table 4**. The $R^2$ and RMSE values of the generated model are given in **Table 5**. These parameters seem to indicate that the model is statistically significant. Hence, the model has been used to produce contour plots that enumerate the relationship between the process parameters and the electrochemical corrosion rate.

**Effect of process parameters on the electrochemical corrosion rate:**

- **Effect of TRS and SD**

The contour plot, as shown in **Figure 11 (d)**, explains the impact of TRS and SD on the electrochemical corrosion rate. As the TRS increases, the electrochemical corrosion rate of the specimens also increases. But the electrochemical corrosion rate decreases with an increase in SD. From the contour plots, it is evident that FSP of specimens at a TRS range of 750 rpm to 850 rpm and SD range of 12 mm to 14 mm results in a high electrochemical corrosion rate (above 11 mils/year. A minimum electrochemical corrosion rate below 2 mils/year has been observed in the specimens processed at TRS below 700 rpm and SD above 16 mm.

- **Effect of TRS and TTS**

**Figure 11 (e)** describes the effect of the TRS and TTS on the electrochemical corrosion rate of the specimens. A simultaneous increase in TRS and TTS has increased the electrochemical corrosion rate. The contour plots show a high electrochemical corrosion rate above 11 mils/year in the specimens processed at a TRS range of 750 rpm to 850 rpm and a TTS range of 24 mm/min to 30 mm/min. The electrochemical corrosion rate of below 1 mils/year has been found in the specimens processed at TRS below 700 and TTS below 14 mm/min.

- **Effect of TTS and SD**

The contour plot represented in **Figure 11 (f)** represents the influence of the process parameters TTS and SD on the electrochemical corrosion rate. An increase in TTS has increased the electrochemical corrosion rate of the specimens. However, the electrochemical corrosion rate has decreased with an increase in SD. A high electrochemical corrosion rate above 11 mils/year has been observed in the specimens processed at a TTS range of 24 mm/min to 30 mm/min and an SD range of 12 mm to 14 mm. A low electrochemical corrosion rate of below 1 mils/year has been observed in the specimens processed at TTS below 16 mm/min and SD above 16 mm.

**Inference – Electrochemical Potential and Electrochemical Corrosion Rate**

A more positive corrosion potential indicates a more pronounced cathodic behaviour of the specimens. Conventionally, the fine dispersion of the sub-micron β phase results in a more perceptible cathodic behaviour. A fine dispersion of β phase results in a lower intergranular corrosion (IGC) effect. Hence, such behavior is expected to reduce the corrosion rate of the specimens. A more negative corrosion potential indicates a more pronounced anodic behavior of the specimens. Agglomeration of β phase creates a significant change in cathodic to anodic surface area, thereby resulting in more IGC. Consequently, a more negative corrosion potential is expected to increase the corrosion rate of the specimens. The presence of more grain boundaries (active sites for corrosion) in fine-grained specimens tends to increase the corrosion rate. However, corrosion of a material is a complex phenomenon that does not only depend on the electrochemical parameters. Surface potential (based on electron work function) also influences the corrosion rate of the specimens. Also, the electrochemical corrosion potential depends on the grain size (intimately with grain boundary) and morphology and distribution of the β phase particles. Similar to the observations of the earlier research work (Vaira Vignesh et al., 2018, Ramalingam et al., 2019, Ramalingam and Ramasamy, 2017, Aravind et al., 2019), the FSPed specimens had also exhibited a non-linear relationship between corrosion potential and corrosion rate. Therefore the process window for simultaneously maximising cathodic behavior and minimising the corrosion rate would be delusive. The process window for minimising the corrosion rate is as follows: TRS range below 700 rpm, TTS below 16 mm/min, and SD value ranging from 16 mm to 18 mm. The process window for maximising the anodic behavior is as follows: TRS range of 550 rpm to 750 rpm, TTS range of 19 mm/min to 27 mm/min, and SD value ranging from 15 mm to 17 mm.

**Electrochemical corrosion surface morphology and elemental composition analysis**

The corroded FSP08 and FSP14 specimens after electrochemical corrosion have been observed under a scanning electron microscope. The surface morphology of the FSP08 and FSP14 specimens observed by the FE-SEM analysis is shown in **Figure 12**. **Figure 12 (a)** and **Figure 12 (b)** show the least corrosion in the FSP08 specimen after electrochemical corrosion. The grey patches in the morphology indicate the corrosion sites. The corrosion products formed on the surface were dissolved in the course of electrochemical corrosion analysis. **Figure 12 (c)** and **Figure 12 (d)** show the typical corroded surface morphology of the high corrosion rate FSP14 specimen. Corrosion products have been observed on the surface of the specimen FSP as white and grey patches. The glassy and lustrous region in the corroded FSPed specimen could be oxide compounds.

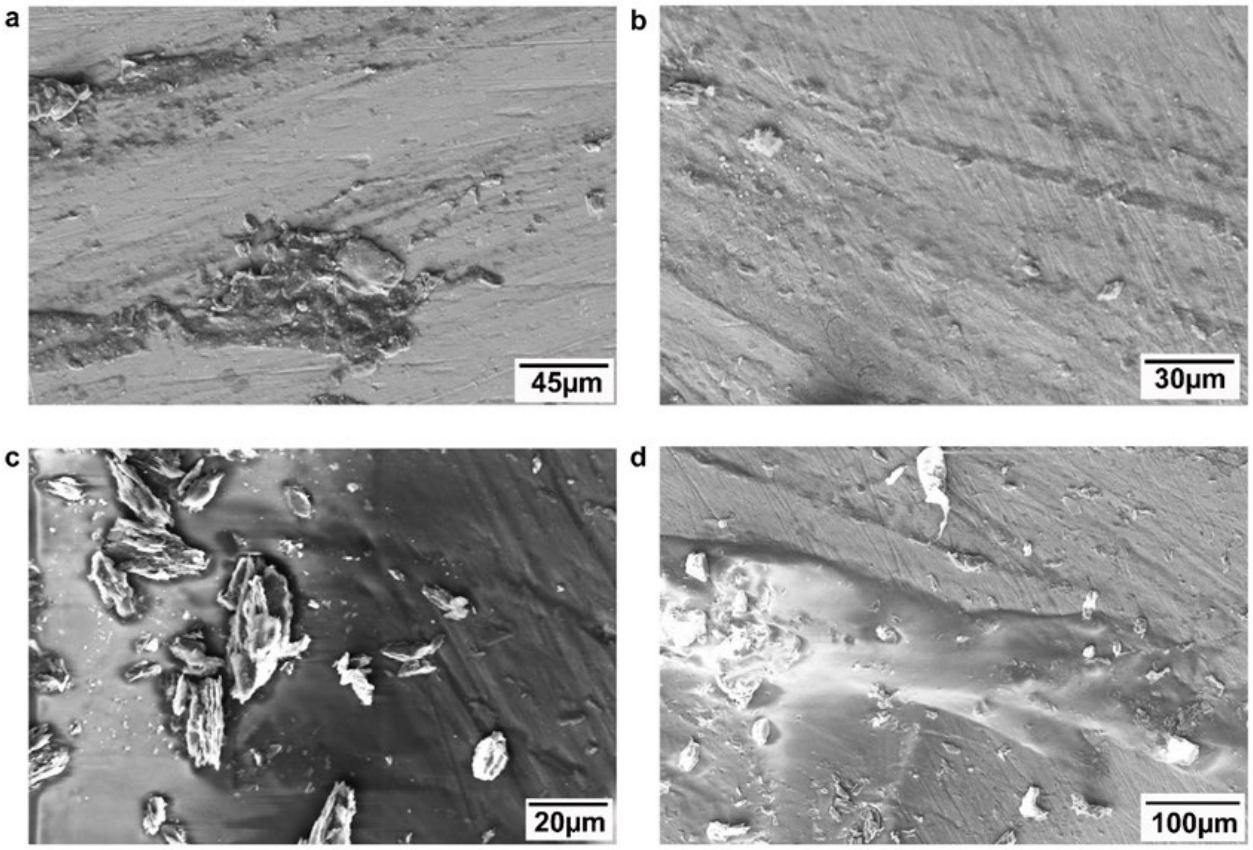


Figure 12. The electrochemical corrosion surface morphology images of:
a) and b) FSP08; c) and d) FSP14 specimens

**Figure 13 (a)** and **Figure 13 (b)** show the elemental composition of the FSP08 and FSP14 specimens after electrochemical corrosion. The elements present have been identified as Al, Mg, Cl, Na, O. The EDS spectrograph of the FSP08 specimen identified the presence of elements Al (91.49 wt.%), O (5.56 wt.%), Mg (2.59 wt.%), and Na and Cl in negligible amounts. The elements Al and O have been more, and Na and Cl, less present in the corrosion layers. The excessive Na, Mg, and Cl have been dissolved or worn off into the electrolyte. Thus the corrosion products that may possibly be deposited on the surface are $AlCl_3$, $Al_2O_3$, or, much less, NaCl, MgO, and $MgCl_2$. A meagre quantity of Cl has been observed on the specimen FSP08, which could be attributed to the high solubility of $AlCl_3$. The EDS spectrograph of specimen FSP14 indicates the elements such as Al (68.49 wt.%), O (12.86 wt.%), Mg (2.01 wt.%), Cl (16.46%), and Na in negligible amounts. The corrosion products that may possibly be deposited on the surface are $AlCl_3$, $Al_2O_3$, or, much less, NaCl, $MgCl_2$, and MgO. The high concentration of elemental O indicates a possible formation of $Al_2O_3$. The specimen FSP14 have more oxygen content on the surface and that is a clear indication of a high corrosion rate.

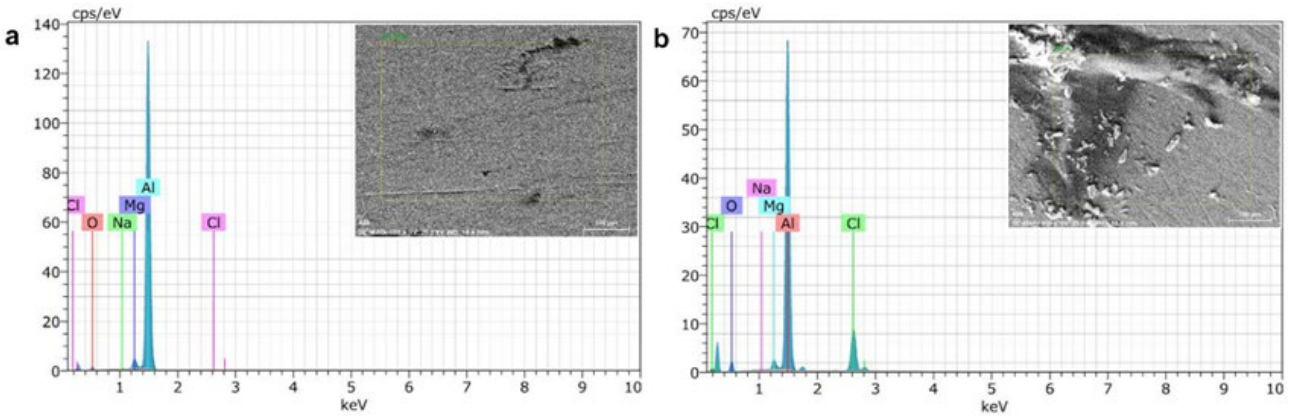


Figure 13. The electrochemical corrosion elemental composition images of a) FSP08 & b) FSP14 specimens

**Electrochemical corrosion mechanism**

$AlCl_3$ and $Al_2O_3$ are dominant corrosion products in the FSPed specimen, as described by electrochemical corrosion analysis. The formation of $AlCl_3$ and $Al_2O_3$ in the electrochemical perspective is shown and elaborated in the **Equation (15) to Equation (20)**. **Equation (15) to Equation (17)** show the reaction of aluminium with water to form $Al_2O_3$. The aluminium reacts with water to form $Al(OH)_3$, as shown in **Equation (15)**. **Equation (16)** shows the formation of $AlO(OH)^+$ ions during the reaction of aluminium with water, which in turn goes into the solution.

$$Al + 3H_2O \rightarrow Al(OH)_3 + 3H^+ + 3e^- \quad (15)$$

$$Al + 2H_2O \rightarrow AlO(OH)^+ + 3H^+ + 3e^- \quad (16)$$

$$Al + (^3/_2)H_2O \rightarrow Al_2O_3 + 3H^+ + 3e^- \quad (17)$$

$$Al(OH)^{2+} + Cl^- \rightarrow Al(OH)Cl^+ \quad (18)$$

$$Al(OH)Cl^+ + H_2O \rightarrow Al(OH)_2Cl + H^+ \quad (19)$$

$$Al(OH)_2Cl + 4Na^+ + 4Cl^- \rightarrow 2AlCl_3 + 4NaOH \quad (20)$$

Aluminium reacts with water to form $Al_2O_3$ , as shown in **Equation (17)**. The aluminium hydroxide is unstable. These aluminium hydroxides form ions and react with chlorine present in NaCl to form $Al(OH)Cl^+$ ions. These ions further react with water to form $Al(OH)_2Cl$. The formed $Al(OH)_2Cl$ is highly unstable. $Al(OH)_2Cl$ then reacts with the $Na^+$ and $Cl^-$ ions present in the electrolyte to form $AlCl_3$. These reactions are clearly explained in **Equation (18) to Equation (20)**. The formation of passivation or protective film of corrosion products has not been observed in the FSPed specimens. Consequently, the corrosion rate has continued, with the dissolution of corrosion products.

## 4. CONCLUSION

FSP trials have been successfully performed on AA5052 alloy. The microstructure, microhardness, wear rate, immersion corrosion rate, and electrochemical corrosion rate have been observed for the base material and FSPed specimen. The effect of process parameters on microhardness, wear rate, immersion corrosion rate, and electrochemical corrosion rate have been investigated. The results of the study are as follows:

- The microstructure of the base material demonstrates the inhomogeneous distribution of coarse β particles. The microstructure of FSP fabricated specimens reveals the refinement of grains, fragmentation, and homogeneous distribution of β phase particles in the α-Al matrix.

- The homogeneously dispersed β particles improve the microhardness and wear resistance of the FSPed specimens more than those of the base material.

- A maximum average microhardness of 73.78 HV (12.61% higher than the base material) has been observed in the specimen FSP12, fabricated at TRS of 700 rpm, TTS of 20 mm/min, and SD of 18 mm.

- A minimum wear rate of $0.2206 \times 10^{-7}$ g/Nm (83.10% lesser than the base material) has been observed in the specimen FSP06, fabricated at a TRS of 900 rpm, TTS of 10 mm/min, and SD of 18 mm.

- The least immersion corrosion rate of 0.0824 mm/year (13% lesser than the base material) has been observed in the specimen FSP05, fabricated at TRS of 500 rpm, TTS of 10 mm/min, and SD of 15 mm.

- The average corrosion potential of the base material has been observed as -1.279 V. A more positive corrosion potential of -0.908 V has been found in the specimen FSP03 fabricated and more negative corrosion potential of -1.465 V in the specimen FSP07.

- A minimum electrochemical corrosion rate of 0.79 mils/year (79.37% lesser than the base material) has been observed in the specimen FSP08, processed at TRS, TTS, and SD of 900 rpm, 30 mm/min, and 18 mm respectively.

- The fine grains and uniform dispersion of β particles reduce the active sites for corrosion in the FSPed specimens. Furthermore, the uneven β particles in the base material cause more active corrosion sites, thereby increasing the corrosion rate. This behaviour has been observed both in immersion corrosion and electrochemical corrosion tests.

## CONFLICT OF INTEREST

The author(s) declared no potential conflicts of interest with respect to the research, authorship, and/or publication of this article.

## GLOSSARY

FSP - Friction Stir Processing

TMAZ - Thermo-Mechanically Affected Zone

FSPed - Friction Stir Processed

TRS - Tool Rotation Speed

TTS - Tool Traverse Speed

SD - Shoulder Diameter

PD - Pin Diameter

ANN - Artificial Neural Network

RBF - Radial Basis Function

XRD - X-Ray Diffraction

SEM - Scanning Electron Microscopy

OCP - Open Circuit Potential

## REFERENCES


Abioye, T. et al., 2019. Prediction of the tensile strength of aluminium alloy 5052-H32 fibre laser weldments using regression analysis. The International Journal of Advanced Manufacturing Technology, 102, 1951-1962.

Alex, A. J. et al., 2020. Effect of heat treatment on the mechanical and wear behavior of friction stir processed AA5052 alloy. Materials Today: Proceedings, 22, 3340-3346.

Anil Kumar, R. et al., 2019. Investigations on the Tribological Properties of Heat-Treated Copper Composite Using Hybrid Quadratic–Radial Basis Function Model. Transactions of the Indian Institute of Metals, 72, 3117-3128.

Aravind, A. Y. et al., 2019. Study on the Mechanical and Corrosion behavior of AA5052 Tailor Welded Blanks Fabricated using Friction Stir Welding. Journal of Materials and Environmental Sciences, 10, 624-636.

Arjun, K. et al., 2019. Effect of load, sliding distance and sliding velocity on the wear properties of aluminum alloy AA5052. IOP Conference Series: Materials Science and Engineering. IOP Publishing, 012016.

Arun Kumar, R. et al, 2021. Examination of the mechanical, corrosion, and tribological behavior of friction stir welded aluminum Alloy AA8011. Transactions on Maritime Science, 10, 20-41.

Ashjari, M. et al., 2015. Experimental investigation on the effect of process environment on the mechanical properties of AA5083/Al2O3 nanocomposite fabricated via friction stir processing. Materials Science and Engineering: A, 645, 40-46.

Awad, O. M. et al., 2018. Production and characterization of AA7075-graphite composite using friction stir processing. Journal of Petroleum and Mining Engineering, 20, 101-110.

Barath, V. et al., 2018. Analysing the strength of friction stir welded dissimilar aluminium alloys using Sugeno Fuzzy model. IOP Conference Series: Materials Science and Engineering. IOP Publishing, 012043.

Bhardwaj, V. et al., 2021. Investigations on the Mechanical and Tribological Performance of Nickel Aluminum Bronze-CaCO3 Composite.

Bodaghi, M. & Dehghani, K. 2017. Friction stir welding of AA5052: the effects of SiC nano-particles addition. The International Journal of Advanced Manufacturing Technology, 88, 2651-2660.

Byung-Wook, A. et al., 2012. Fabrication of SiCp/AA5083 composite via friction stir welding. Transactions of Nonferrous Metals Society of China, 22, s634-s638.

Chanakyan, C. et al., 2021. Optimization of FSP process parameters on AA5052 employing the S/N ratio and ANOVA method. Advances in Materials Science and Engineering.

Chen, Y. et al., 2003. The effect of extrusion temperature on the development of deformation microstructures in 5052 aluminium alloy processed by equal channel angular extrusion. Acta Materialia, 51, 2005-2015.

Davis, J., 1999. Corrosion of Aluminum and Aluminum Alloys", ASM International. Chen, JH, Costan, E., van Huis, MA, Xu, Q. & Zandbergen, HW Atomic pillar-based nanoprecipitates strengthen AlMgSi alloys. Science, 312,416-419.

Davis, J. R., 1993. Aluminum and aluminum alloys, ASM international.

Dolatkhah, A. et al., 2012. Investigating effects of process parameters on microstructural and mechanical properties of Al5052/SiC metal matrix composite fabricated via friction stir processing. Materials & Design, 37, 458-464.

Hariri, M. B. et al., 2013. The optimum combination of tool rotation rate and traveling speed for obtaining the preferable corrosion behavior and mechanical properties of friction stir welded AA5052 aluminum alloy. Materials & Design, 50, 620-634.

Howeyze, M. et al., 2018. Effects of deformation routes on the evolution of microstructure, texture and tensile properties of AA5052 aluminum alloy. Materials Science and Engineering: A, 732, 120-128.

Huang, C. et al., 2016. Effect of tool rotation speed on microstructure and microhardness of friction-stir-processed cold-sprayed SiCp/Al5056 composite coating. Journal of Thermal Spray Technology, 25, 1357-1364.

Jalili, N. et al., 2016. Experimental and numerical study of simultaneous cooling with CO2 gas during friction stir welding of Al-5052. Journal of Materials Processing Technology, 237, 243-253.

Jayakarthick, C. et al., 2018. Analysing the influence of FSP process parameters on IGC susceptibility of AA5083 using Sugeno - Fuzzy model.

Kiruthi Murugan, C. B. et al., 2018. Friction surfacing mild-steel with Monel and predicting the coating parameters using fuzzy logic. 16402-16410.

Kumar, N. et al., 2011. The effect of friction stir processing on the microstructure and mechanical properties of equal channel angular pressed 5052Al alloy sheet. Journal of materials science, 46, 5527-5533.

Mirjavadi, S. S. et al., 2017. Effect of multi-pass friction stir processing on the microstructure, mechanical and wear properties of AA5083/ZrO2 nanocomposites. Journal of Alloys and Compounds, 726, 1262-1273.

Mondolfo, L. F., 2013. Aluminum alloys: structure and properties, Elsevier.

Murugan, B. K. et al., 2018. Study of the effect of parameters in friction surfacing of Monel over Mild Steel using linear - Radial basis function model. 8604-8611.

Murugesan, M. et al., 2021. Experimental and numerical investigation of AA5052-H32 Al alloy with U-Profile in cold roll forming. Materials, 14, 470.

Padmanaban, R. et al., 2014. Numerical simulation of temperature distribution and material flow during friction stir welding of dissimilar aluminum alloys. Procedia Engineering, 97, 854-863.

Prabhakar, G. et al., 2018. Surface metal matrix composites of Al5083-fly ash produced by friction stir processing. Materials Today: Proceedings, 5, 8391-8397.

Premkumar, R. et al., 2021. Investigation on the microstructure, microhardness, and tribological behavior of AA1100-hBN surface composite. Koroze a Ochrana Materialu, 65, 1-11.

Prudhvi Sai, P. et al., 2021. Artificial neural network models for predicting the corrosion behavior of friction stir processed AA5083. 7215-7219.

Qin, Z., et al., 2019. Synergistic effect of hydroxylated boron nitride and silane on corrosion resistance of aluminum alloy 5052. Journal of the Taiwan Institute of Chemical Engineers, 100, 285-294.

Ramalingam, V. V. & Ramasamy, P., 2017. Modelling Corrosion Behavior of Friction Stir Processed Aluminium Alloy 5083 Using Polynomial: Radial Basis Function. Transactions of the Indian Institute of Metals, 70, 2575-2589.

Ramalingam, V. V. et al., 2019. Microstructure, hardness and corrosion behaviour of friction-stir processed AA5083. Anti-Corrosion Methods and Materials, 66, 791-801.

Seyed Salehi, M. & Anjabin, N., 2017. Modeling and experimental study of static recovery and mechanical behavior of AA5052 alloy during cold-working and subsequent annealing. Iranian Journal of Materials Forming, 4, 28-38.

Shahraki, S. et al., 2013. Producing of AA5083/ZrO2 nanocomposite by friction stir processing (FSP). Metallurgical and Materials Transactions B, 44, 1546-1553.

Shanavas, S. & Dhas, J. E. R., 2017. Weldability of AA 5052 H32 aluminium alloy by TIG welding and FSW process–a comparative study. IOP Conference Series: Materials Science and Engineering. IOP Publishing, 012016.

Sharifitabar, M. et al., 2011. Fabrication of 5052Al/Al2O3 nanoceramic particle reinforced composite via friction stir processing route. Materials & Design, 32, 4164-4172.

Sherif, K. & Narayan, R. 1989. Electrochemical behaviour of aluminium in 1M NaCl solution: Part 1: Open circuit potential measurements. British Corrosion Journal, 24, 199-203.

Sinyavskii, V. & Kalinin, V. 2005. Marine corrosion and protection of aluminum alloys according to their composition and structure. Protection of metals, 41, 317-328.

Spacht, R. B., 1946. The corrosion resistance of aluminum and its alloys. Journal of Chemical Education, 23, 253.

Suganya Priyadharshini, G. et al., 2021. Influence of tool traverse speed on microstructure and mechanical properties of CuNi/B4C surface composites. Transactions of the Institute of Metal Finishing, 99, 38-45.

Vaira Vignesh, R. & Padmanaban, R., 2018. Artificial neural network model for predicting the tensile strength of friction stir welded aluminium alloy AA1100. 16716-16723.

Vaira Vignesh, R. et al., 2018. Influence of FSP on the microstructure, microhardness, intergranular corrosion susceptibility and wear resistance of AA5083 alloy. Tribology - Materials, Surfaces and Interfaces, 12, 157-169.

Vaira Vignesh, R. et al., 2019a. Investigations on the surface topography, corrosion behavior, and biocompatibility of friction stir processed magnesium alloy AZ91D. Surface Topography: Metrology and Properties, 7.

Vaira Vignesh, R. et al., 2019b. Mechanical properties and corrosion behaviour of AZ91D-HAP surface composites fabricated by friction stir processing. Materials Research Express, 6.

Vaira Vignesh, R. et al., 2020. Study on the corrosion and wear characteristics of magnesium alloy AZ91D in simulated body fluids. Bulletin of Materials Science, 43.

Vignesh, R. V. & Padmanaban, R., 2018a. Intergranular corrosion susceptibility of friction stir processed aluminium alloy 5083. Materials today: proceedings, 5, 16443-16452.

Vignesh, R. V. & Padmanaban, R., 2018b. Modelling of peak temperature during friction stir processing of magnesium alloy AZ91. IOP Conference Series: Materials Science and Engineering. IOP Publishing, 012019.

Vignesh, R. V. et al., 2016. Numerical modelling of thermal phenomenon in friction stir welding of aluminum plates.

Vignesh, R. V. et al., 2018. Soft computing model for analysing the effect of friction stir processing parameters on the intergranular corrosion susceptibility of aluminium alloy AA5083. Koroze a Ochrana Materialu, 62, 97-107.

Vignesh, R. V. et al., 2020. Corrosion protection of magnesium alloys in simulated body fluids using nanophase Al2O3. Corrosion Protection at the Nanoscale. Elsevier.

Wahid, M. A. et al., 2020. Aluminum alloys in marine construction: characteristics, application, and problems from a fabrication viewpoint. Marine Systems & Ocean Technology, 15, 70-80.

Yuvaraj, N. & Aravindan, S. 2015. Fabrication of Al5083/B4C surface composite by friction stir processing and its tribological characterization. Journal of materials research and technology, 4, 398-410.